J. Fluid Mech. (2013), *vol.* 733, *pp.* 33–67.
doi:10.1017/jfm.2013.432

Instabilities of natural convection in a periodically heated layer

M. Z. Hossain‡ and J. M. Floryan†

Department of Mechanical and Materials Engineering, The University of Western Ontario, London, ON, Canada N6A 5B9

(Received 2 March 2013; revised 7 July 2013; accepted 9 August 2013; first published online 19 September 2013)

Natural convection in an infinite horizontal layer subject to periodic heating along the lower wall has been investigated using a combination of numerical and asymptotic techniques. The heating maintains the same mean temperatures at both walls while producing sinusoidal temperature variations along one horizontal direction, with its spatial distribution characterized by the wavenumber α and the amplitude expressed in terms of a Rayleigh number Ra_p. The primary response of the system takes the form of stationary convection consisting of rolls with the axis orthogonal to the heating wave vector and structure determined by the particular values of Ra_p and α. It is shown that for sufficiently large α convection is limited to a thin layer adjacent to the lower wall with a uniform conduction zone emerging above it; the temperature in this zone becomes independent of the heating pattern and varies in the vertical direction only. Linear stability of the above system has been considered and conditions leading to the emergence of secondary convection have been identified. Secondary convection gives rise to either longitudinal rolls, transverse rolls or oblique rolls at the onset, depending on α. The longitudinal rolls are parallel to the primary rolls and the transverse rolls are orthogonal to the primary rolls, and both result in striped patterns. The oblique rolls lead to the formation of convection cells with aspect ratio dictated by their inclination angle and formation of rhombic patterns. Two mechanisms of instability have been identified. In the case of $\alpha = O(1)$, parametric resonance dominates and leads to a pattern of instability that is locked in with the pattern of heating according to the relation $\delta_{cr} = \alpha/2$, where δ_{cr} denotes the component of the critical disturbance wave vector parallel to the heating wave vector. The second mechanism, the Rayleigh–Bénard (RB) mechanism, dominates for large α, where the instability is driven by the uniform mean vertical temperature gradient created by the primary convection, with the critical disturbance wave vector $\delta_{cr} \to 1.56$ for $\alpha \to \infty$ and the fluid response becoming similar to that found in the case of a uniformly heated wall. Competition between these mechanisms gives rise to non-commensurable states in the case of longitudinal rolls and the appearance of soliton lattices, to the formation of distorted transverse rolls, and to the appearance of the wave vector component in the direction perpendicular to the forcing direction. A rapid stabilization is observed when the heating wavenumber is reduced below $\alpha \approx 2.2$ and no instability is found when $\alpha < 1.6$ in the range of Ra_p considered. It is shown that α plays the

† Email address for correspondence: mfloryan@eng.uwo.ca

‡ Current address: Department of Mechanical Engineering, Bangladesh University of Engineering and Technology (BUET), Dhaka-1000, Bangladesh.

role of an effective pattern control parameter and its judicious selection provides a means for the creation of a wide range of flow responses.

Key words: buoyancy-driven instability, convection

1. Introduction

The understanding of motions of fluids over geometrically, chemically and thermally patterned surfaces is of vital interest in designing microfluidic components and devices for biological applications such as cell analysers. Of particular importance is how convective motions develop and, in the case of droplets, how they move along regularly structured surfaces (Beltrame *et al.* 2011). The same issues are relevant in the development of hydrophilic surfaces. Beltrame *et al.* (2011) find seven distinct transition regimes for interface depinning. This diversity shows that, in addition to requiring a clear understanding of the different kinds of surface heterogeneities that may cause the pinning, the complex coupling between pinning force and surface of the fluid needs to be taken into account.

Patterned heating offers the potential to produce structured convection, which provides an alternative to geometric patterning. The structure of convection may be directly related to the pattern of heating or it could be dictated by secondary states. The determination of conditions leading to secondary states, as well as the determination of the pattern of this convection and its relation to the pattern of heating, represents the first step in the development of potential applications. An understanding of patterned convection is required for reliable prediction of local contaminant transport in urban environments. This transport is driven by different heating rates associated with colour variations of roofs, streets and parks. Similar conditions can be encountered in rural environments, where local circulation can be driven by different heating rates of patterns of forests and lakes. Transport processes in the presence of patterns of heat sources, such as systems of localized fires, heated computer chips, and so on, represent further potential applications.

Most of the existing works deal with convection in a uniformly heated layer, so-called Rayleigh–Bénard (RB) convection (Bodenschatz, Pesch & Ahlers 2000). Motion occurs when the Rayleigh number Ra, based on the mean temperature difference between the bounding walls, exceeds a critical value. This motion takes the form of rolls (striped pattern) and is characterized by a linear neutral stability curve with a well-defined minimum which identifies the critical Rayleigh number Ra_c and the critical wave vector $\boldsymbol{q}_c$. Linear stability theory does not offer any guidelines regarding the spontaneous pattern selection which, in most experiments, is determined by secondary effects. Competition between rolls and spatiotemporally chaotic states such as spiral-defect chaos has also been observed (Bodenschatz *et al.* 2000). The onset of convection can be modified by externally imposed forcing. When spatially distributed one-dimensional forcing is used, the system may exhibit wavenumber locking and responses that extend into two spatial dimensions, allowing for a wide resonance range (Manor, Hagberg & Meron 2008, 2009). Two types of distributed forcing have been considered: (i) spatially modulated geometry, and (ii) spatially modulated wall temperature. In both cases only small-amplitude modulations have been allowed, due to interest in control/alteration of the pattern selection of RB convection.

Results dealing with RB convection in modulated geometry are very limited. McCoy *et al.* (2008) used thin stripes glued on the lower surface characterized by the wavenumber $\boldsymbol{q}_m$ and oriented along a selected direction, where $\boldsymbol{q}_m$ varied in a small interval around $|\boldsymbol{q}_c|$. Two-dimensional rolls with the wave vector $\boldsymbol{q}_m$ were observed for $Ra \ll Ra_c$. These rolls grew in amplitude with Ra until they were destabilized, with the dominant mechanisms being dependent on the ratio of $\boldsymbol{q}_m$ and $\boldsymbol{q}_c$. The wave vectors of the resulting modes formed a non-zero angle with the modulation wave vector $\boldsymbol{q}_m$, leading to the formation of oblique modes and producing a variety of three-dimensional patterns. Seiden *et al.* (2008) combined the effect of a gravity-induced shear flow and spatially one-dimensional forcing created by surface strips. Both anisotropies cooperated when the strips were parallel to the flow, resulting in the formation of longitudinal rolls, and competed when the angle between the respective wave vectors increased to 90°. A variety of novel patterns was observed. The effects of spatial temperature modulations have been studied by Freund, Pesch & Zimmermann (2011), who added small-amplitude sinusoidal temperature variations to the lower wall. The system response consisted of a weak primary convection induced by the temperature modulations and instabilities driven by the mean temperature gradient. When $q_m \approx q_c$, the RB pattern locked in with the modulation and the rolls remained stable for fairly large $Ra > Ra_c$. For q_m slightly less than q_c, the secondary motion developed in the form of cross-roll and oscillatory instabilities (Seiden *et al.* 2008). For q_m slightly larger than q_c, skewed-varicose instability appeared and, at the same time, the Eckhaus and zigzag instabilities were suppressed. Several modes of instability directly associated with the modulation were identified for q_m away from q_c and with $Ra \approx Ra_c$. For q_m less than $0.8q_c$, the instability involved two oblique rolls (Clever & Busse 1974; Vozovoi & Nepomnyashchy 1974). The same response was found for $1.2q_c < q_m < 2q_c$. Longitudinal rolls became dominant for $2q_c < q_m < 2.08q_c$ and were replaced by transverse rolls for a still larger q_m. Effects of a combination of modulated geometry and temperatures have been considered by Schmitz & Zimmerman (1996) in the limit of long wavelength modulations. The analysis demonstrated the existence of steady two-dimensional drifts, with the drift pattern depending on the relative phase between modulations. The onset of convection changed from steady to oscillatory at well-defined ratios of the modulation wavenumbers and the relative phases.

Convection driven by a periodic heating in the absence of mean temperature gradient has not attracted much attention. Fluid motion is driven by horizontal density gradients and occurs regardless of the intensity of the heating. Its pattern is determined by the externally imposed heating pattern unless transition to secondary states is encountered. The net heat transfer between the walls is driven by the nonlinear effects and has been studied by Hossain & Floryan (2013) for a wide range of Prandtl numbers. Its magnitude is a function of the heating pattern, with the largest heat flow occurring for the heating wavenumber $\alpha \approx 1$ and dropping off rapidly for smaller and higher α. The same heating applied to moving fluid results in the reduction of drag experienced by this fluid. This so-called super-thermohydrophobic effect (Floryan 2012) has been described in detail by Hossain, Floryan & Floryan (2012), and relies on the formation of small separation bubbles that isolate the moving stream from direct contact with the solid wall and thus reduce the shear stress acting on the fluid. The fluid movement inside separation bubbles is partially driven by the buoyancy gradients associated with the heating, which further contributes to the reduction of the required pressure drop.

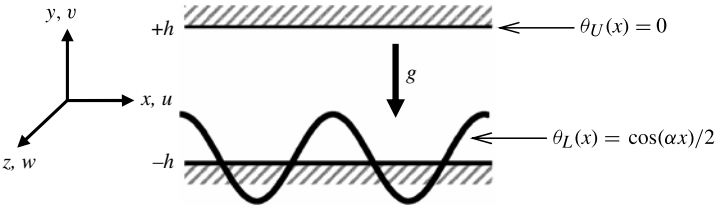

FIGURE 1. Fluid layer subject to periodic heating.

The present work is focused on the analysis of system dynamics when a stationary fluid layer is exposed to periodic heating, with the main interest being the determination of conditions leading to the onset of secondary states and identification of the form of the resulting convection. It should be stressed that there is no reference wavenumber, as in the case of RB convection, as the wave vector of the primary convection is dictated by the heating. There is also no reference critical Rayleigh number, as the primary convection sets in regardless of the intensity of the heating. The Rayleigh number Ra used in RB convection becomes irrelevant, as there is no externally imposed mean temperature difference. One can, however, introduce a Rayleigh number Ra_p based on the amplitude of spatial temperature modulations, and use it as a measure of intensity of the heating, with Ra and Ra_p being unrelated. Transition to secondary states may result in motions with patterns seemingly unrelated to patterns of the heating. The results provide a reference point for analysis of flow systems driven by other forms of spatially distributed forcing, as the current literature deals with very simple model problems only (Manor *et al.* 2008, 2009).

The paper is organized as follows. Section 2 provides a description of the primary convection. The method of solution is discussed in § 2.1 and the flow and temperature fields are described in § 2.2. Section 3 is devoted to analysis of the linear stability of this convection. Formulation of the stability problem is presented in § 3.1, the method of solution is discussed in § 3.2, and a description of the secondary convection is provided in § 3.3. In particular, longitudinal rolls are discussed in § 3.3.1, transverse rolls are discussed in § 3.3.2 and arbitrary, oblique rolls are discussed in § 3.3. Section 4 provides a short summary of the main conclusions.

2. Primary convection

Consider buoyancy-driven movement of fluid contained between two horizontal parallel plates extending to $\pm\infty$ in the x and z directions and placed at a distance $2h$ apart with the gravitational acceleration g acting in the negative y direction, as shown in figure 1. The fluid is incompressible, Newtonian, with thermal conductivity k_d, specific heat per unit mass c, thermal diffusivity $\kappa = k_d/\rho c$, kinematic viscosity ν, dynamic viscosity μ, thermal expansion coefficient Γ and variations of the density ρ which follow the Boussinesq approximation. All material properties are taken at the reference temperature defined below. The lower wall is subject to a heating periodic in the x direction with the wavelength $\lambda = 2\pi/\alpha$ while the upper one is kept isothermal, i.e.

$$\theta_L(x) = \tfrac{1}{2}\cos(\alpha x), \quad \theta_U(x) = 0. \tag{2.1}$$

In the above, $\theta = T - T_{ref}$ denotes the relative temperature, T denotes the absolute temperature, T_{ref} denotes the reference temperature (temperature of the upper wall),

subscripts L and U refer to the lower and upper walls, respectively, and the factor $1/2$ has been added to bring the amplitude of temperature variations to unity.

The complete temperature field is decomposed into a sum of the conductive part θ_{cond} and modifications θ_1 due to convection. The amplitude of temperature variation along the lower wall is used as the conductive temperature scale T_d and $T_v = T_d\nu/\kappa$ is used as the convective temperature scale, where $T_v/T_d = Pr$ and $Pr = \nu/\kappa$ denotes the Prandtl number. The half-distance h between the walls is used as the length scale, $U_v = \nu/h$ as the (convective) velocity scale and $P_v = \rho U_v^2$ as the (dynamic) pressure scale.

The complete temperature field is scaled using the convective scale resulting in

$$\Theta_1(x, y) = Pr^{-1}\theta_{cond}(x, y) + \theta_1(x, y), \tag{2.2}$$

where the conductive part θ_{cond} represents the solution of the Laplace problem subject to boundary conditions (2.1) and has the form

$$\theta_{cond}(x, y) = \theta_c(y)\cos(\alpha x) = \frac{1}{4}\left[\frac{\cosh(\alpha y)}{\cosh(\alpha)} - \frac{\sinh(\alpha y)}{\sinh(\alpha)}\right]\cos(\alpha x), \tag{2.3}$$

and the convective part is a function of x and y only due to the form of the heating. Separation of the temperature field into conductive and convective parts assists in identification of instability mechanisms discussed in § 3. The dimensionless field equations for the two-dimensional velocity and temperature modifications take the form

$$u_1\frac{\partial u_1}{\partial x} + v_1\frac{\partial u_1}{\partial y} = -\frac{\partial p_1}{\partial x} + \nabla^2 u_1, \tag{2.4a}$$

$$u_1\frac{\partial v_1}{\partial x} + v_1\frac{\partial v_1}{\partial y} = -\frac{\partial p_1}{\partial y} + \nabla^2 v_1 + Ra_p\theta_1 + Ra_p Pr^{-1}\theta_{cond}, \tag{2.4b}$$

$$Pr\left(u_1\frac{\partial \theta_1}{\partial x} + v_1\frac{\partial \theta_1}{\partial y}\right) + u_1\frac{\partial \theta_{cond}}{\partial x} + v_1\frac{\partial \theta_{cond}}{\partial y} = \nabla^2\theta_1, \tag{2.4c}$$

$$\frac{\partial u_1}{\partial x} + \frac{\partial v_1}{\partial y} = 0, \tag{2.4d}$$

where $\boldsymbol{v}_1 = (u_1, v_1)$ denotes the velocity vector, p_1 stands for the pressure, $Ra_p = g\Gamma h^3 T_d/\nu\kappa$ is the Rayleigh number and ∇^2 denotes the Laplace operator. The boundary conditions have the form

$$u_1(\pm 1) = 0, \quad v_1(\pm 1) = 0, \quad \theta_1(\pm 1) = 0. \tag{2.5}$$

2.1. *Method of solution*

The stream function $\psi_1(x, y)$ is introduced in the usual manner, i.e. $u_1 = \partial\psi_1/\partial y$, $v_1 = -\partial\psi_1/\partial x$, and pressure is eliminated from the momentum equations resulting in

$$\frac{\partial\psi_1}{\partial y}\frac{\partial}{\partial x}\left(\nabla^2\psi_1\right) - \frac{\partial\psi_1}{\partial x}\frac{\partial}{\partial y}\left(\nabla^2\psi_1\right) = \nabla^4\psi_1 - Ra_p\frac{\partial\theta_1}{\partial x} - Ra_p Pr^{-1}\frac{\partial\theta_{cond}}{\partial x}, \tag{2.6a}$$

$$Pr\left(\frac{\partial\psi_1}{\partial y}\frac{\partial\theta_1}{\partial x} - \frac{\partial\psi_1}{\partial x}\frac{\partial\theta_1}{\partial y}\right) + \frac{\partial\psi_1}{\partial y}\frac{\partial\theta_{cond}}{\partial x} - \frac{\partial\psi_1}{\partial x}\frac{\partial\theta_{cond}}{\partial y} = \nabla^2\theta_1. \tag{2.6b}$$

The solution is assumed to be in the form of Fourier expansions:

$$\psi_1 = \sum_{n=-\infty}^{n=+\infty}\varphi_1^{(n)}(y)e^{in\alpha x}, \quad \theta_1 = \sum_{n=-\infty}^{n=+\infty}\phi_1^{(n)}(y)e^{in\alpha x}, \tag{2.7}$$

where $\varphi_1^{(n)} = \varphi_1^{(-n)*}$, $\phi_1^{(n)} = \phi_1^{(-n)*}$ represent the reality conditions and asterisks denote complex conjugates. Substitution of (2.7) into (2.6) and separation of Fourier components results in the following system of nonlinear ordinary differential equations:

$$\mathrm{D}_n^2\varphi_1^{(n)} - \mathrm{i}n\alpha\, Ra_p\phi_1^{(n)} - \mathrm{i}\alpha\sum_{m=-\infty}^{m=+\infty}[m\,\mathrm{D}\varphi_1^{(n-m)}\mathrm{D}_m\varphi_1^{(m)} - (n-m)\,\varphi_1^{(n-m)}\mathrm{D}_m(\mathrm{D}\varphi_1^{(m)})]$$
$$= \mathrm{i}\,n\,\alpha\, Ra_p Pr^{-1}\delta_{1|n|}\theta_c, \tag{2.8a}$$

$$\mathrm{D}_n\phi_1^{(n)} - \mathrm{i}\alpha\sum_{m=-\infty}^{m=+\infty}[Pr(m\phi_1^{(m)}\mathrm{D}\varphi_1^{(n-m)} - (n-m)\,\varphi_1^{(n-m)}\mathrm{D}\phi_1^{(m)})$$
$$+ (m\delta_{1|m|}\theta_c\mathrm{D}\varphi_1^{(n-m)} - (n-m)\,\varphi_1^{(n-m)}\delta_{1|m|}\mathrm{D}\theta_c)] = 0, \tag{2.8b}$$

where $-\infty < n < +\infty$, $\mathrm{D} = \mathrm{d}/\mathrm{d}y$ and $\mathrm{D}_n = \mathrm{D}^2 - n^2\alpha^2$ and $\delta_{1|n|}$ stands for the Kronecker delta. The required boundary conditions have the form

$$\varphi_1^{(n)}(\pm 1) = 0, \quad \mathrm{D}\varphi_1^{(n)}(\pm 1) = 0, \quad \phi_1^{(n)}(\pm 1) = 0 \quad \text{for } -\infty < n < +\infty. \tag{2.9a–c}$$

System (2.8), together with boundary conditions (2.9a–c), needs to be solved numerically. The solution method uses variable step-size, finite difference discretization based on the Simpson method with deferred corrections (Kierzenka & Shampine 2001, 2008), with the resulting algebraic system solved using a simplified Newton (chord) method with residual control. Selection of the number and distribution of grid points is done automatically to meet the specified error bounds. The number of Fourier modes used in the solution has been selected via numerical experiment in order to provide at least six-digit accuracy. Results were matched, when required, with Hossain & Floryan (2013), in which a different method was used. In the post-processing stage, the velocity field is evaluated according to the relation

$$v_1(x,y) = \sum_{n=-\infty}^{n=+\infty}[f_{1u}^{(n)}(y), f_{1v}^{(n)}(y), 0]\mathrm{e}^{\mathrm{i}n\alpha x} = \sum_{n=-\infty}^{n=+\infty}[\mathrm{D}\varphi_1^{(n)}, -\mathrm{i}n\alpha\varphi_1^{(n)}, 0]\mathrm{e}^{\mathrm{i}n\alpha x}. \tag{2.10}$$

2.2. *Description of the flow and temperature fields*

The structure of the conductive temperature field (2.3) demonstrates that the space between the walls is separated into heated and cooled zones creating horizontal pressure variations. A stationary system with such a pressure distribution is never statically stable, and thus convection occurs regardless of the intensity of the heating. The topology of the flow consists of pairs of counter-rotating rolls, as illustrated in figure 2, with fluid rising above the hot spots at the lower wall. When Ra_p increases, the centres of the rolls move upwards and towards the hot zones. An increase of α brings the centres of the rolls closer to the lower wall.

The results displayed in figure 3 demonstrate that the strength of the rolls, as measured by the maximum of the stream function ψ_{1max}, increases approximately linearly with Ra_p (for a fixed α) and begins to saturate for $Ra_p > 10^3$. This growth can be predicted analytically, as shown in the Appendix. The strength of the rolls decreases in proportion to α^{-3} (for a fixed Ra_p) when α is large enough. The character of the flow field in the latter case can also be predicted analytically by noting that the

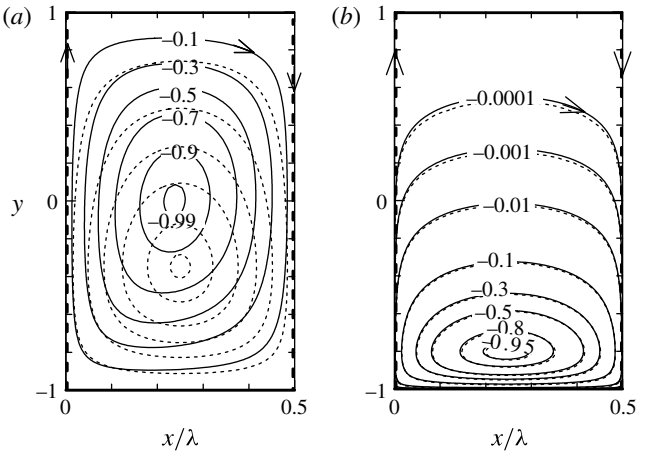

FIGURE 2. Flow topology for $Ra_p = 1$ (dotted lines) and $Ra_p = 10^4$ (solid lines). The stream function is normalized with its maximum $\psi_{1,max}$: (*a*) results for $\alpha = 3$ ($\psi_{1,max} = 0.0017$, 10.43 for $Ra_p = 1$, 10^4), (*b*) results for $\alpha = 10$ ($\psi_{1,max} = 4.77 \times 10^{-5}$, 0.4683 for $Ra_p = 1$, 10^4).

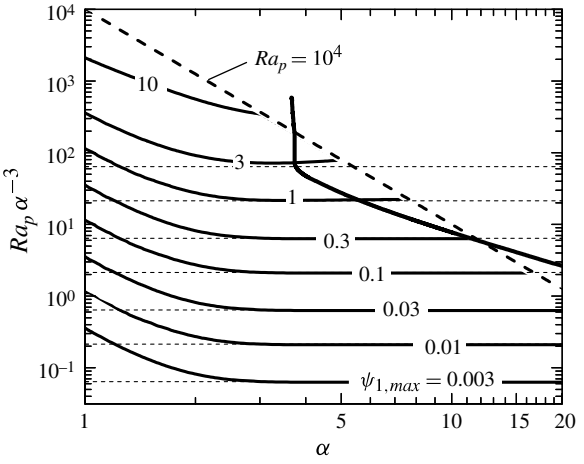

FIGURE 3. Variations of the maximum of the stream function $\psi_{1,max}$ as a function of α and Ra_p/α^3. The dashed line corresponds to the maximum of Ra_p considered. Asymptotes determined on the basis of (2.16) are illustrated using dotted lines. The thick solid line identifies critical stability conditions for the longitudinal rolls.

conductive temperature field takes the form

$$\theta_{cond}(x, y) = \tfrac{1}{2}\mathrm{e}^{-\alpha(1+y)}\cos(\alpha x) \tag{2.11}$$

for $\alpha \to \infty$, i.e. it forms a boundary layer adjacent to the lower wall. The buoyancy force that drives the motion is active only in this layer. Analysis of this case begins with rescaling of the x-coordinate with the heating wavelength $X = \alpha x$, and the solution of (2.4) is sought using the method of matched asymptotic expansions. Since the boundary layer is concentrated next to the lower wall, the stretched variable Y is

defined as $Y=\alpha(1+y)$. The inner solution is assumed to be of the form

$$\left.\begin{aligned} u_1&=\alpha^{-2}\tilde{U}_2+\alpha^{-3}\tilde{U}_3+\alpha^{-4}\tilde{U}_4+\alpha^{-5}\tilde{U}_5+0(\alpha^{-6}),\\ v_1&=\alpha^{-2}\tilde{V}_2+\alpha^{-3}\tilde{V}_3+\alpha^{-4}\tilde{V}_4+\alpha^{-5}\tilde{V}_5+0(\alpha^{-6}),\end{aligned}\right\} \tag{2.12a}$$

$$\left.\begin{aligned} p_1&=\alpha^{-1}\tilde{P}_1+\alpha^{-2}\tilde{P}_2+\alpha^{-3}\tilde{P}_3+\alpha^{-4}\tilde{P}_4+0(\alpha^{-5}),\\ \theta_1&=\alpha^{-3}\tilde{\Theta}_3+\alpha^{-4}\tilde{\Theta}_4+\alpha^{-5}\tilde{\Theta}_5+\alpha^{-6}\tilde{\Theta}_6+0(\alpha^{-7}),\end{aligned}\right\} \tag{2.12b}$$

and is substituted into (2.4) expressed in terms of the (X, Y) variables, and the same order terms are extracted. The leading-order system has the form

$$O(\alpha^{-2}):\ -\frac{\partial\tilde{P}_1}{\partial X}+\frac{\partial^2\tilde{U}_2}{\partial X^2}+\frac{\partial^2\tilde{U}_2}{\partial Y^2}=0,\quad -\frac{\partial\tilde{P}_1}{\partial Y}+\frac{\partial^2\tilde{V}_2}{\partial X^2}+\frac{\partial^2\tilde{V}_2}{\partial Y^2}+Ra_pPr^{-1}\theta_{cond}=0,$$

$$\frac{\partial\tilde{U}_2}{\partial X}+\frac{\partial\tilde{V}_2}{\partial Y}=0,\quad \tilde{U}_2=\tilde{V}_2=0\quad \text{at } Y=0,\ \tilde{U}_2,\tilde{V}_2\to 0 \text{ as } Y\to\infty. \tag{2.13}$$

Its solution has the form

$$\left.\begin{aligned} u_1&=-2^{-4}\alpha^{-2}Ra_p\,Pr^{-1}\,(2-Y)\,Y\mathrm{e}^{-Y}\sin(X)+0(\alpha^{-5}),\\ v_1&=2^{-4}\,\alpha^{-2}Ra_p\,Pr^{-1}\,Y^2\mathrm{e}^{-Y}\cos(X)+0(\alpha^{-5}),\end{aligned}\right\} \tag{2.14}$$

where the error term will be discussed later. Convection at this level of approximation is proportional to Ra_p but Ra_p cannot be too large ($Ra_p<\alpha^2$) for approximation to be valid. The leading-order approximation for the stream function becomes

$$\psi_1=-2^{-4}\alpha^{-3}Ra_p\,Pr^{-1}\,Y^2\mathrm{e}^{-Y}\sin(X)+0(\alpha^{-6}). \tag{2.15}$$

The maximum of the stream function can be readily computed as

$$\psi_{1,max}=0.25\mathrm{e}^{-2}Ra_p\alpha^{-3}Pr^{-1}=0.04765Ra_p\alpha^{-3} \tag{2.16}$$

and provides a basis for determination of asymptotes displayed in figure 3. The location of this maximum at $y=2\alpha^{-1}-1$ identifies the location of the vortex centre as well as the rate of its approach to the lower wall when α increases. The above results demonstrate explicitly that the spatial structure of convection for $\alpha\to\infty$ is dominated by the heating wavelength.

The topology of the temperature field is more complex. For weak heating, the field is nearly identical to the field given by the conduction component (2.3) (see figure 4*a*). An increase of Ra_p leads to the formation of saddle points (see figure 4*b*), an increase of the size of plumes over the hot spots and temperature rise of the bulk of the fluid. For high enough Ra_p, the temperature field splits into two distinct horizontal layers (see figure 4*c*), the lower layer characterized by strong horizontal modulations which will be referred to as the convection layer, and the upper layer exhibiting negligible horizontal temperature variations which will be referred to as the conduction layer. Further increase of Ra_p leads to the upward penetration of convection and disappearance of the conduction layer (see figure 4*d*). The evolution of the temperature field is qualitatively similar for different values of α but the quantitative differences can be significant. In the case of α being $O(1)$, e.g. $\alpha=3$ (figure 5*a,b*), plumes of heated fluid are well pronounced, cooled fluid occupies relatively less space and formation of the conduction layer is not observed. In the case of large α, e.g. $\alpha=10$ (figure 5*c,d*), formation of the conduction layer is observed for Ra_p as low as $Ra_p=O(10^2)$.

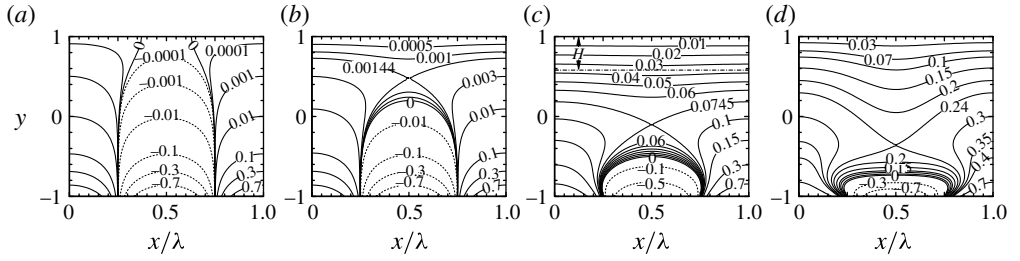

FIGURE 4. Temperature field Θ_1 normalized by its maximum $\Theta_{1,max} = (2Pr)^{-1}$ for $\alpha = 5$: (*a*) $Ra_p = 10$; (*b*) $Ra_p = 10^2$; (*c*) $Ra_p = 2 \times 10^2$; (*d*) $Ra_p = 10^4$. The solid (dashed) lines identify positive (negative) temperatures.

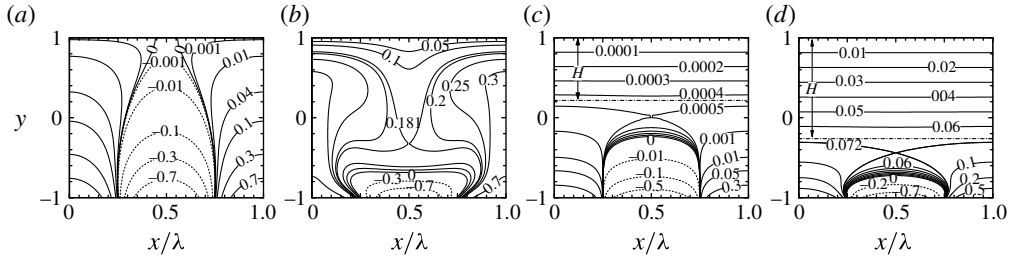

FIGURE 5. Temperature field Θ_1: (*a*,*b*) $\alpha = 3$, (*c*,*d*) $\alpha = 10$; (*a*,*c*) $Ra_p = 10^2$, (*b*,*d*) $Ra_p = 10^4$. H denotes the thickness of the conduction layer (see also figure 7). Other parameters are the same as in figure 4.

The structure of the temperature field for $\alpha \to \infty$ can be determined by substituting (2.12) into (2.4) and extracting system $O(\alpha^{-3})$, which is of the form

$$-\frac{\partial \tilde{P}_2}{\partial X} + \frac{\partial^2 \tilde{U}_3}{\partial X^2} + \frac{\partial^2 \tilde{U}_3}{\partial Y^2} = 0, \quad -\frac{\partial \tilde{P}_2}{\partial Y} + \frac{\partial^2 \tilde{V}_3}{\partial X^2} + \frac{\partial^2 \tilde{V}_3}{\partial Y^2} = 0, \quad \frac{\partial \tilde{U}_3}{\partial X} + \frac{\partial \tilde{V}_3}{\partial Y} = 0, \tag{2.17}$$

$$\frac{\partial^2 \tilde{\Theta}_3}{\partial X^2} + \frac{\partial^2 \tilde{\Theta}_3}{\partial Y^2} = \tilde{U}_2 \frac{\partial \theta_{cond}}{\partial X} + \tilde{V}_2 \frac{\partial \theta_{cond}}{\partial Y},$$

$$\tilde{U}_3 = \tilde{V}_3 = \tilde{\Theta}_3 = 0 \quad \text{at } Y = 0,\ \tilde{U}_3,\ \tilde{V}_3 \to 0 \text{ as } Y \to \infty. \tag{2.18}$$

It is rather obvious that $\tilde{U}_3 = \tilde{V}_3 = 0$. The solution for $\tilde{\Theta}_3$ has the form

$$\tilde{\Theta}_3 = -2^{-7} Ra_p\, Pr^{-1}(Y^2 + Y + 0.5)\mathrm{e}^{-2Y} + CY + 2^{-8} Ra_p\, Pr^{-1}$$
$$+ 2^{-7} Ra_p\, Pr^{-1} Y(Y - 0.5)\mathrm{e}^{-2Y} \cos(2X), \tag{2.19}$$

where the constant C must be determined from matching with the outer solution. Analysis of systems $O(\alpha^{-4})$, $O(\alpha^{-5})$ and energy equations for $O(\alpha^{-6})$ shows that $\tilde{U}_4 = \tilde{V}_4 = \tilde{\Theta}_4 = \tilde{\Theta}_5 = 0$ but $\tilde{U}_5$, $\tilde{V}_5$, $\tilde{\Theta}_6$ are not zero and are proportional to Ra_p^2. The outer problem therefore represents a conduction problem and thus the temperature must be a linear function of y, at least up to $O(\alpha^{-6})$. This leads to the temperature field of the form

$$\theta_1 = \alpha^{-3} Ra_p\, Pr^{-1} 2^{-7} \{[-(Y^2 + Y + 0.5)\mathrm{e}^{-2Y} - 0.25(\alpha^{-1} Y - 2)]$$
$$+ [Y(Y - 0.5)\mathrm{e}^{-2Y}] \cos(2X)\} + 0(\alpha^{-6}), \tag{2.20}$$

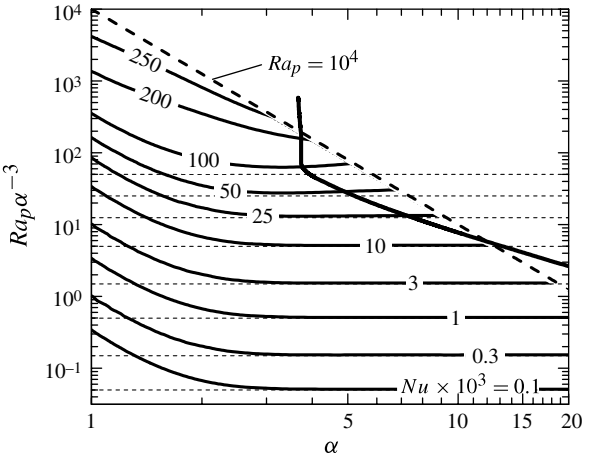

FIGURE 6. Variations of the Nusselt number $Nu \times 10^3$ as a function of α and Ra_p/α^3. The dashed line corresponds to the maximum of Ra_p considered. The dotted lines illustrate asymptotes determined on the basis of (2.22). The thick solid line identifies critical stability conditions for the longitudinal rolls.

which demonstrates that convection in the boundary layer creates a temperature jump between the wall and the outer region at $Y = O(1)$. A temperature gradient across the outer region is generated in order to satisfy the boundary condition at $y = 1$ and this leads to the appearance of the net heat flow between the walls.

The heat flow across the channel can be expressed using the Nusselt number defined by

$$Nu = \frac{Pr}{\lambda}\int_0^{\lambda}\left(-\left.\frac{\mathrm{d}\Theta_1}{\mathrm{d}y}\right|_{y=-1}\right)\mathrm{d}x = -Pr\left.\frac{\mathrm{d}\phi_1^{(0)}}{\mathrm{d}y}\right|_{y=-1}. \tag{2.21}$$

Its variations illustrated in figure 6 demonstrate that Nu increases approximately linearly with Ra_p (for a fixed α) and decreases in proportion to α^{-3} (for a fixed Ra_p), i.e. the character of these variations is similar to variations of $\psi_{1,max}$. This should not be surprising as the heat transport between the walls is driven by convection (see the analysis summarized in the Appendix). The Nusselt number for large enough α can be explicitly evaluated from (2.20) as

$$Nu = 2^{-9}Ra_p\alpha^{-3}, \tag{2.22}$$

which provides a basis for determination of the asymptotes shown in figure 6. Change in the character of heat transfer taking place at $\alpha \approx 4$ suggests a potential difference in the system dynamics for $O(1)$ and large-α regimes. We shall return to this question in § 3.

It is useful to complete this discussion with an explicit quantification of the thickness H of the conduction layer as its variations help to illustrate the interplay between the conductive and convective parts of the temperature field. The thickness can be formally defined using the ratio of the periodic and aperiodic heat flow

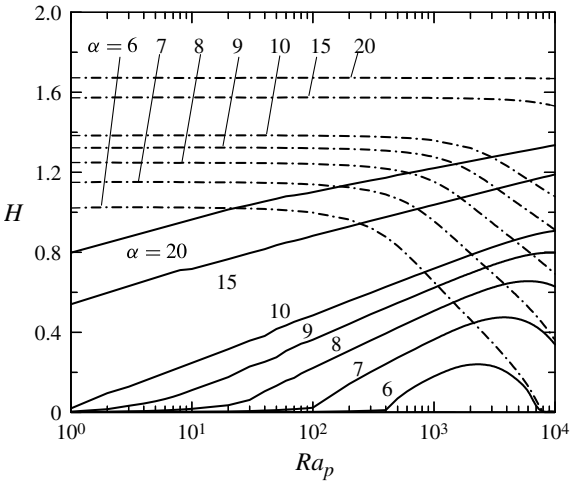

FIGURE 7. Variations of the thickness H of the conduction layer (see figure 4) as a function of α and Ra_p. Solid lines identify H evaluated on the basis of the complete temperature field while dot-dashed lines correspond to H evaluated on the basis of the convective temperature field only.

components, i.e.

$$E = \left\{ \left[Pr^{-1}\alpha(\Theta^{(1)} + \Theta^{(-1)}) + \sum_{n=-\infty, n\neq 0}^{n=\infty} |n|\alpha\phi^{(n)} \right]^2 + \left[Pr^{-1}(\mathrm{D}\Theta^{(1)} + \mathrm{D}\Theta^{(-1)}) + \sum_{n=-\infty, n\neq 0}^{n=\infty} \mathrm{D}\phi^{(n)} \right]^2 \right\}^{1/2} \Big/ |\mathrm{D}\phi^{(0)}|. \quad (2.23)$$

The vertical location corresponding to $E = 0.01$ has been selected to identify the bottom of the conduction layer. The 1 % criterion is rather arbitrary but, nevertheless, it well illustrates the formation of this layer. It is sufficient to use only the first three modes from the convective part of the temperature field as the rate of decay of higher modes with distance away from the wall increases rapidly with the mode number. Figure 7 illustrates variations of H computed on the basis of the complete temperature field and on the basis of the convective part of this field. It can be seen that an increase of Ra_p, while keeping α fixed, initially leads to an increase of H, as an increase in the strength of convective effects reduces the relative importance of spatial modulations caused by the conductive effect. Further increase of Ra_p produces an opposite trend due to an upward penetration of convection. For example, a conductive layer for $\alpha = 7$ begins to form at $Ra_p \approx 10^2$, it reaches its maximum thickness at $Ra_p \approx 4 \times 10^3$ and it begins to shrink with further increase of Ra_p. A judicious selection of Ra_p can therefore lead to either reinforcement or reduction of the spatial modulations, and formation/elimination of the conductive zone is one of the outcomes. It will be shown in the next section that changes in the character of instability represent another outcome of the same process. The character of the system response for a fixed Ra_p but variable α is easier to predict as an increase of α always leads to

an increase of H. It is of interest to note that the main x-modulation of the thermal field in the limit of $\alpha \to \infty$ comes from the conduction effect (see (2.11) and (2.20)).

In the next section, we shall address the question of possible transition of thermal convection described above to secondary states. The fluid layer consists of segments distributed along the x direction, where the conductive temperature field generates either a stabilizing or a destabilizing vertical temperature gradient (see figure 4*a*). The convective motion rearranges these gradients and, generally, increases the fraction of the layer with the unstable gradient (see figures 4 and 5). The magnitude of this gradient increases with an increase of Ra_p, which should lead to an instability if a sufficiently large Ra_p is used. At large α the majority of the layer is occupied by the conductive layer with an unstable temperature gradient and, if this gradient is large enough, a Rayleigh–Bénard-like instability is expected to emerge. At $\alpha = O(1)$ the complex structure of the temperature field prevents one from making predictions without detailed analysis.

3. Linear stability analysis

3.1. *Problem formulation*

The analysis begins with the governing equations in the form of vorticity transport, energy and continuity equations:

$$\frac{\partial \boldsymbol{\omega}}{\partial t} - (\boldsymbol{\omega}\cdot\boldsymbol{\nabla})\,\boldsymbol{v} + (\boldsymbol{v}\cdot\boldsymbol{\nabla})\,\boldsymbol{\omega} = \nabla^2\boldsymbol{\omega} + \boldsymbol{\nabla}\times(Ra_p\theta\boldsymbol{j}), \quad \boldsymbol{\nabla}\cdot\boldsymbol{v} = 0, \quad \boldsymbol{\omega} = \boldsymbol{\nabla}\times\boldsymbol{v}, \tag{3.1a–c}$$

$$\frac{\partial\theta}{\partial t} + (\boldsymbol{v}\cdot\boldsymbol{\nabla})\theta = Pr^{-1}\nabla^2\theta \tag{3.1d}$$

where $\boldsymbol{j}$ is the unit vector along the vertical direction, and $\boldsymbol{\omega}$ and $\boldsymbol{v}$ are the vorticity and velocity vectors, respectively. Unsteady three-dimensional disturbances are superimposed on the base flow in the form (Floryan 1997)

$$\left.\begin{aligned} &\boldsymbol{\omega} = \boldsymbol{\omega}_1(x,y) + \boldsymbol{\omega}_2(x,y,z,t), \quad \boldsymbol{v} = \boldsymbol{v}_1(x,y) + \boldsymbol{v}_2(x,y,z,t),\\ &\theta = Pr^{-1}\theta_{cond}(x,y) + \theta_1(x,y) + \theta_2(x,y,z,t), \end{aligned}\right\} \tag{3.2a–c}$$

where $\boldsymbol{\omega}_1$ is the vorticity vector of the primary convection, the subscript 2 refers to the disturbance fields, $\boldsymbol{v}_2 = (u_2, v_2, w_2)$ is the disturbance velocity vector, $\boldsymbol{\omega}_2 = (\omega_{x2}, \omega_{y2}, \omega_{z2})$ is the disturbance vorticity vector and θ_2 stands for the temperature disturbance. The flow quantities (3.2) are substituted into (3.1), the base part (primary convection) is subtracted, and the equations are linearized. The resulting disturbance equations have the form

$$\frac{\partial\boldsymbol{\omega}_2}{\partial t} + (\boldsymbol{v}_1\cdot\boldsymbol{\nabla})\boldsymbol{\omega}_2 - (\boldsymbol{\omega}_2\cdot\boldsymbol{\nabla})\boldsymbol{v}_1 + (\boldsymbol{v}_2\cdot\boldsymbol{\nabla})\boldsymbol{\omega}_1 - (\boldsymbol{\omega}_1\cdot\boldsymbol{\nabla})\boldsymbol{v}_2 = \nabla^2\boldsymbol{\omega}_2 + \boldsymbol{\nabla}\times(Ra_p\theta_2\boldsymbol{j}), \tag{3.3a}$$

$$\boldsymbol{\nabla}\cdot\boldsymbol{v}_2 = 0, \quad \boldsymbol{\omega}_2 = \boldsymbol{\nabla}\times\boldsymbol{v}_2, \quad \frac{\partial\theta_2}{\partial t} + (\boldsymbol{v}_2\cdot\boldsymbol{\nabla})\Theta_1 + (\boldsymbol{v}_1\cdot\boldsymbol{\nabla})\theta_2 = Pr^{-1}\nabla^2\theta_2 \tag{3.3b–d}$$

and are subject to the homogeneous boundary conditions

$$\boldsymbol{v}_2 = 0, \quad \theta_2 = 0 \tag{3.3e}$$

at the walls. The disturbance equations (3.3) have coefficients that are functions of x and y, and thus the solution can be written in the form

$$\boldsymbol{\omega}_2(x,y,z,t) = \boldsymbol{\Omega}_2(x,y)\mathrm{e}^{\mathrm{i}(\delta x+\beta z-\sigma t)} + \text{c.c.} \quad \boldsymbol{v}_2(x,y,z,t) = \boldsymbol{V}_2(x,y)\mathrm{e}^{\mathrm{i}(\delta x+\beta z-\sigma t)} + \text{c.c.}, \tag{3.4a,b}$$

$$\theta_2(x,y,z,t) = \Theta_2(x,y)\mathrm{e}^{\mathrm{i}(\delta x+\beta z-\sigma t)} + \text{c.c.} \tag{3.4c}$$

The disturbance wave vector has components (δ, β) in the (x, z) directions, $\boldsymbol{\Omega}_2(x, y)$, $\boldsymbol{V}_2(x, y)$ and $\Theta_2(x, y)$ are the x-periodic amplitude functions modulated by the heating, the exponent σ is assumed to be complex ($\sigma = \sigma_r + \mathrm{i}\sigma_i$) and its imaginary and real parts describe the rate of growth and the frequency of disturbances, respectively, and c.c. stands for the complex conjugate. Positive σ_i identifies instability. The x-periodicity of the base flow is determined by the imposed heating.

Set (δ, β, σ) represents eigenvalues for the specified heating conditions (Pr, Ra, α) creating a large parameter space. The relevant eigenvalue problem for the partial differential equations (3.3) can be easily derived. Rather than solving this problem directly, we take advantage of the periodicity of the amplitude functions and represent them in terms of Fourier expansions,

$$\left.\begin{aligned}
\boldsymbol{\Omega}_2(x,y) &= \mathrm{i}\sum_{m=-\infty}^{m=+\infty}[\zeta_{2x}^{(m)}(y), \zeta_{2y}^{(m)}(y), \zeta_{2z}^{(m)}(y)]\mathrm{e}^{\mathrm{i}m\alpha x},\\
\boldsymbol{V}_2(x,y) &= \sum_{m=-\infty}^{m=+\infty}[g_{2u}^{(m)}(y), g_{2v}^{(m)}(y), g_{2w}^{(m)}(y)]\mathrm{e}^{\mathrm{i}m\alpha x},\\
\Theta_2(x,y) &= \sum_{m=-\infty}^{m=+\infty} g_{2\theta}^{(m)}(y)\mathrm{e}^{\mathrm{i}m\alpha x},
\end{aligned}\right\} \tag{3.5a–c}$$

which leads to the following form of the disturbance quantities:

$$\boldsymbol{\omega}_2(x,y,z,t) = \mathrm{i}\sum_{m=-\infty}^{m=+\infty}[\zeta_{2x}^{(m)}(y), \zeta_{2y}^{(m)}(y), \zeta_{2z}^{(m)}(y)]\mathrm{e}^{\mathrm{i}[(\delta+m\alpha)x+\beta z-\sigma t]} + \text{c.c.}, \tag{3.6a}$$

$$\boldsymbol{v}_2(x,y,z,t) = \sum_{m=-\infty}^{m=+\infty}[g_{2u}^{(m)}(y), g_{2v}^{(m)}(y), g_{2w}^{(m)}(y)]\mathrm{e}^{\mathrm{i}[(\delta+m\alpha)x+\beta z-\sigma t]} + \text{c.c.}, \tag{3.6b}$$

$$\theta_2(x,y,z,t) = \sum_{m=-\infty}^{m=+\infty} g_{2\theta}^{(m)}(y)\,\mathrm{e}^{\mathrm{i}[(\delta+m\alpha)x+\beta z-\sigma t]} + \text{c.c.} \tag{3.6c}$$

Substitution of (3.6) into (3.3) and separation of Fourier components results, after rather lengthy algebra, in a system of linear homogeneous ordinary differential equations in the form

$$A^{(m)}\zeta_{2y}^{(m)} = \sum_{n=-\infty}^{n=+\infty}[H_\zeta^{(m-n)}\zeta_{2y}^{(m-n)} + H_v^{(m-n)}g_{2v}^{(m-n)}], \tag{3.7a}$$

$$B^{(m)}g_{2v}^{(m)} - Ra_p k_m^2 g_{2\theta}^{(m)} = -\sum_{n=-\infty}^{n=+\infty}[I_\zeta^{(m-n)}\zeta_{2y}^{(m-n)} + I_v^{(m-n)}g_{2v}^{(m-n)}], \tag{3.7b}$$

$$C^{(m)}g_{2\theta}^{(m)} = Pr\sum_{n=-\infty}^{n=+\infty}[J_\zeta^{(m-n)}\zeta_{2y}^{(m-n)} + J_v^{(m-n)}g_{2v}^{(m-n)} + J_\theta^{(m-n)}g_{2\theta}^{(m-n)}], \tag{3.7c}$$

subject to boundary conditions

$$\left.\begin{array}{l} \zeta_{2y}^{(m)}(\pm 1)=0, \quad g_{2v}^{(m)}(\pm 1)=0, \quad \mathrm{D}g_{2v}^{(m)}(\pm 1)=0, \\ g_{2\theta}^{(m)}(\pm 1)=0 \quad \text{for } -\infty < m < +\infty, \end{array}\right\} \tag{3.8}$$

where

$$\left.\begin{array}{l} A^{(m)}=\mathrm{D}^2-k_m^2+\mathrm{i}\sigma, \quad B^{(m)}=(\mathrm{D}^2-k_m^2)^2+\mathrm{i}\sigma(\mathrm{D}^2-k_m^2), \\ C^{(m)}=\mathrm{D}^2-k_m^2+\mathrm{i}Pr\sigma, \quad t_m=\delta+m\alpha, \quad k_m^2=t_m^2+\beta^2, \end{array}\right\} \tag{3.9a}$$

$$H_\zeta^{(m-n)}=it_m f_{1u}^{(n)}+k_{m-n}^{-2}(\beta^2+t_{m-n}t_m)f_{1v}^{(n)}\mathrm{D}, \quad H_v^{(m-n)}=-\beta\mathrm{D}f_{1u}^{(n)}+\mathrm{i}n\alpha\beta k_{m-n}^{-2}f_{1v}^{(n)}\mathrm{D}^2, \tag{3.9b}$$

$$I_\zeta^{(m-n)}=n\alpha\beta k_{m-n}^{-2}[2t_{m-n}f_{1u}^{(n)}\mathrm{D}+(t_m+t_{m-n})\mathrm{D}f_{1u}^{(n)}-\mathrm{i}k_m^2 f_{1v}^{(n)}-if_{1v}^{(n)}\mathrm{D}^2], \tag{3.9c}$$

$$\begin{aligned} I_v^{(m-n)}=&\,k_{m-n}^{-2}[\mathrm{i}n\alpha(\beta^2-t_m t_{m-n})\mathrm{D}f_{1u}^{(n)}\mathrm{D}+k_m^2(\beta^2+t_{m-n}t_{m-2n})f_{1v}^{(n)}\mathrm{D}] \\ &+k_{m-n}^{-2}[\mathrm{i}(-k_{m-n}^2 t_m+2n\alpha\beta^2)f_{1u}^{(n)}\mathrm{D}^2+(n\alpha\, t_m-k_m^2)f_{1v}^{(n)}\mathrm{D}^3] \\ &+\mathrm{i}k_m^2 t_{m-2n}f_{1u}^{(n)}+\mathrm{i}t_m\mathrm{D}^2 f_{1u}^{(n)}, \end{aligned} \tag{3.9d}$$

$$\left.\begin{array}{l} J_\zeta^{(m-n)}=-\mathrm{i}n\alpha\beta k_{m-n}^{-2}(\phi_1^{(n)}+\delta_{1|n|}\theta_c), \\ J_v^{(m-n)}=-n\alpha k_{m-n}^{-2}t_{m-n}(\phi_1^{(n)}+\delta_{1|n|}\theta_c)\mathrm{D}+\mathrm{D}(\phi_1^{(n)}+\delta_{1|n|}\theta_c), \end{array}\right\} \tag{3.9e}$$

$$J_\theta^{(m-n)}=it_{m-n}f_{1u}^{(n)}+f_{1v}^{(n)}\mathrm{D}. \tag{3.9f}$$

The above formulation is analogous to the Bloch theory (Bloch 1928) for systems with spatially periodic coefficients. It can also be interpreted in terms of Floquet's theory (Coddington & Levinson 1965).

3.2. *Method of solution*

Equations (3.7*a–c*) together with the boundary conditions (3.8) are truncated after N_M modes. The dispersion relation is determined numerically by solution of the relevant eigenvalue problem. For the purposes of calculations, the problem is posed as an eigenvalue problem for σ. Equations (3.7*a–c*) are discretized with spectral accuracy using the Chebyshev collocation method with N_T collocation points. The discretization procedure results in a matrix eigenvalue problem $\Xi x=0$, where $\Xi(\sigma)$ represents the coefficient matrix. This matrix is linear in σ, i.e. $\Xi=\Xi_0+\Xi_1\sigma$, where $\Xi_0=\Xi(0)$, $\Xi_1=\Xi(1)-\Xi_0$. The σ-spectrum is determined by solving a general eigenvalue problem in the form $\Xi_0 x=\sigma\Xi_1 x$. The individual eigenvalues are determined by finding zeros of the determinant of Ξ. The computed eigenvalues are further refined using the inverse iteration technique.

Two methods for tracing the eigenvalues in the parameter space have been used (Floryan 2003). In the first method, we alter the flow conditions and produce an approximation for the eigenvalue, which is then improved iteratively by searching for the nearby zero of the determinant using a Newton–Raphson search procedure. A reasonable guess for the unknown eigenvalue is essential for the convergence. In the second method, the inverse iterations method, we compute an approximation for the eigenvector Λ_a corresponding to the unknown eigenvalue σ_a using an iterative process in the form $(\Xi_0-\sigma_0\Xi_1)\Lambda^{(k+1)}=\Xi_1\Lambda^{(k)}$, where σ_0 and $\Lambda^{(0)}$ are the eigenvalue and the eigenvector (an eigenpair) corresponding to the unaltered flow. If σ_a is the eigenvalue closest to σ_0, then $\Lambda^{(k)}$ converges to Λ_a. The eigenvalue σ_a is evaluated using formula $\sigma_a=\Lambda_a^*\Xi_0\Lambda_a/\Lambda_a^*\Xi_1\Lambda_a$, where the asterisk denotes the complex conjugate transpose. The inverse iterations method was found to be generally more efficient. The relevant

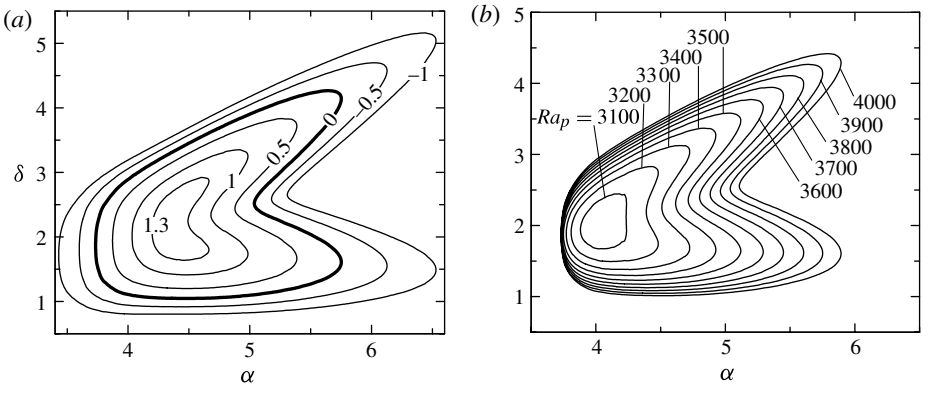

FIGURE 8. (*a*) Variations of the amplification rate $\mathrm{Im}(\sigma)$ of longitudinal rolls for $Ra_p = 3900$ and (*b*) variations of the neutral stability conditions for a fixed Ra_p as a function of the heating wavenumber α and the roll wavenumber δ.

numerical parameters (i.e. N_M and N_T) have been selected via numerical convergence studies to guarantee at least four-digit eigenvalue accuracy.

Various test calculations and scans through the parameter space in the range of α and Ra_p of interest identified only stationary disturbances, i.e. $\mathrm{Re}(\sigma) = 0$, which are referred to as rolls. A description of the critical stability conditions, the structure of the disturbance motion and how the instability responds to changes in the spatial pattern of heating is given in the next section for fluid with Prandtl number $Pr = 0.71$, which closely approximates the properties of air.

3.3. *Onset of the secondary convection*

The primary rolls are characterized by the wave vector $\boldsymbol{q}_m = (\alpha, 0)$, i.e. they are aligned in the z direction, resulting in a system with translational symmetry. The form and orientation of the disturbance structures are uncertain. This discussion begins with two reference structures, i.e. the longitudinal rolls, which are aligned along the primary rolls, and the transverse rolls, which are orthogonal to the primary rolls, as this provides a means for simple identification and description of the dominant mechanisms. We conclude the presentation with a description of the most general case, i.e. oblique rolls, which give rise to the formation of convection cells.

3.3.1. *Longitudinal rolls*

Longitudinal rolls are characterized by the wave vector $\boldsymbol{q} = (\delta, 0)$, i.e. they have axes parallel to the axes of the primary rolls. The flow system retains translation symmetry.

Figure 8(*a*) displays variations of the amplification rate of the rolls as a function of α and the roll wavenumber δ for $Ra_p = 3900$. It extends over several Brillouin zones in the δ direction in order to explicitly demonstrate how the leading eigenvalue is affected by the heating pattern. There exists a finite range of α, which results in instability. The range of wavelengths of the rolls that may emerge from the instability is also finite, with the most amplified wavenumber corresponding to $\delta \approx 2$. Figure 8(*b*) displays a set of neutral curves for a sequence of Ra_p. It can be seen that a decrease in the heating intensity (decrease of Ra_p) results in the reduction of the range of heating patterns that can lead to instability and, at the same time, reduction in the range of the

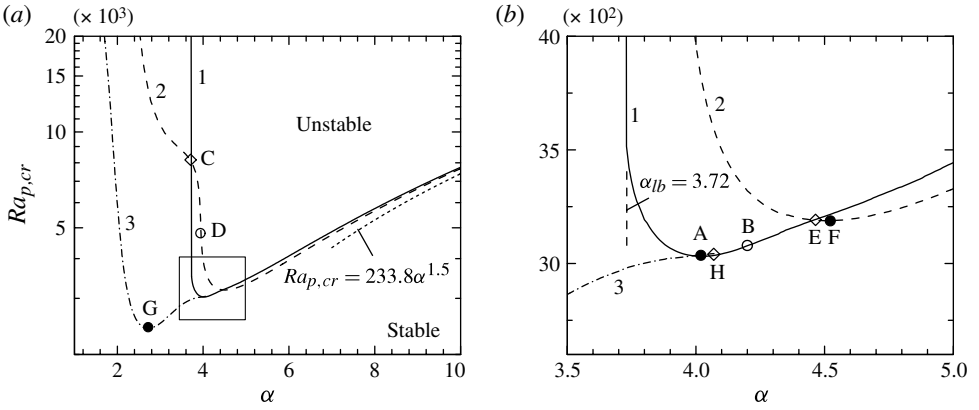

FIGURE 9. Variations of the critical Rayleigh number $Ra_{p,cr}$ as a function of α. A close-up of the box in (*a*) is displayed in (*b*). Curves 1, 2, 3 correspond to the longitudinal, transverse and oblique rolls, respectively. Locations of points: A, $Ra_A = 3031.6$, $\alpha_A = 4.03$; B, $Ra_B = 3078.3$, $\alpha_B = 4.2$; C, $Ra_C = 8099.0$, $\alpha_C = 3.72$; D, $Ra_D = 4823.9$, $\alpha_D = 3.95$; E, $Ra_E = 3191.8$, $\alpha_E = 4.46$; F, $Ra_F = 3188.6$, $\alpha_F = 4.51$; G, $Ra_G = 2411.2$, $\alpha_G = 2.69$; H, $Ra_H = 3043.6$, $\alpha_H = 4.07$.

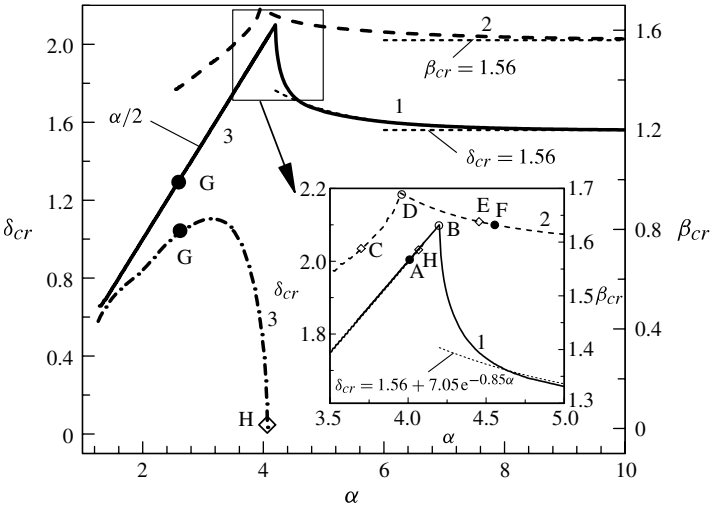

FIGURE 10. Variations of the critical wavenumbers δ_{cr} and β_{cr} as functions of α. Curves 1, 2, 3 correspond to the longitudinal, transverse and oblique rolls, respectively. Locations of points, corresponding to the same points in figure 9: A, $\alpha_A = 4.03$, $\delta_A = 2.015$; B, $\alpha_B = 4.2$, $\delta_B = 2.1$; C, $\alpha_C = 3.72$, $\beta_C = 1.59$; D, $\alpha_D = 3.95$, $\beta_D = 1.69$; E, $\alpha_E = 4.46$, $\beta_E = 1.64$; F, $\alpha_F = 4.51$, $\beta_F = 1.63$; G, $\alpha_G = 2.69$, $\delta_G = 1.345$, $\beta_G = 0.8$; H, $\alpha_H = 4.07$, $\delta_H = 2.035$, $\beta_H = 0$.

roll wavenumbers δ that can be produced by the instability. Detailed analysis shows that the instability does not occur for $Ra_p < 3031.6$ (see point A in figure 9).

One can identify the upper and lower limits of the unstable range of α for each value of Ra_p and the corresponding values of δ to produce the plots displayed in figures 9–10. These plots identify the critical conditions leading to

the onset of instability. There is a certain minimum heating intensity defined by $Ra_{p,min} = Ra_A = 3031.6$ (point A in figure 9*b*), along with an associated very specific heating pattern corresponding to $\alpha_{min} = \alpha_A = 4.03$, that is required in order to initiate the instability. An increase of Ra_p above 3031.6 increases the range of the unstable heating patterns. The critical curve rises steeply when α is reduced below α_{min} and, as a matter of fact, this instability does not occur when $\alpha < \alpha_{lb} = 3.72$ in the range of Ra_p considered. Since the most intense convection occurs at $\alpha \approx 1$ (see § 2), one may conclude that the stabilization is related to the increase of the intensity of convection. An increase of α above $\alpha_A = 4.03$ results in a gradual increase of $Ra_{p,cr}$, which eventually follows an asymptote (see figure 9*a*). It has been shown in § 2 that increase of α generally reduces the intensity of convection, but a combination of increase of α and increase of Ra_p keeps convective effects at a level sufficient to produce instability. It can be summarized that the spatial heating pattern corresponding to $\alpha_{min} = \alpha_A = 4.03$ is the most efficient at inducing the longitudinal roll instability and any other pattern requires more intense heating. Heating patterns with sufficiently small α are unable to create longitudinal rolls.

The explanation of the mechanics of roll formation starts with analysis of the limit $\alpha \to \infty$. Since the neutral conditions are of interest, system (2.4) provides the starting point with $q_1(x, y) \to q_1(x, y) + q_2(x, y)$, where $q_1(x, y)$ stands for the basic state determined in § 2 and $q_2(x, y)$ represents a small disturbance. Substitution of flow quantities into (2.4) and linearization lead to the disturbance equation of the form

$$u_1\frac{\partial u_2}{\partial x} + u_2\frac{\partial u_1}{\partial x} + v_1\frac{\partial u_2}{\partial y} + v_2\frac{\partial u_1}{\partial y} = -\frac{\partial p_2}{\partial x} + \nabla^2 u_2, \tag{3.10a}$$

$$u_2\frac{\partial v_1}{\partial x} + u_1\frac{\partial v_2}{\partial x} + v_1\frac{\partial v_2}{\partial y} + v_2\frac{\partial v_1}{\partial y} = -\frac{\partial p_2}{\partial y} + \nabla^2 v_2 + Ra_p\theta_2, \tag{3.10b}$$

$$Pr\left(u_1\frac{\partial \theta_2}{\partial x} + v_1\frac{\partial \theta_2}{\partial y}\right) + Pr\left(u_2\frac{\partial \theta_1}{\partial x} + v_2\frac{\partial \theta_1}{\partial y}\right) + \left(u_2\frac{\partial \theta_{cond}}{\partial x} + v_2\frac{\partial \theta_{cond}}{\partial y}\right) = \nabla^2\theta_2, \tag{3.10c}$$

$$\frac{\partial u_2}{\partial x} + \frac{\partial v_2}{\partial y} = 0. \tag{3.10d}$$

The last term in (3.10*b*) provides a coupling between the temperature and the flow fields. The redistribution of the temperature field is described by (3.10*c*), where the first bracket describes modifications of the temperature disturbance field due to the primary convection, the second bracket describes modifications of the disturbance velocity field due to the primary convective temperature field, the third bracket describes contributions to the disturbance temperature field associated with modulations of the conductive temperature field, and the right-hand side describes the conduction process that balances all convective effects. In the limit $\alpha \to \infty$, θ_{cond} is given by (2.11), u_1 and v_1 are given by (2.14), and θ_1 is given by (2.20). If the boundary layer is ignored, $(u_1,\ v_1,\ \theta_{cond},\ \partial\theta_1/\partial x) \to 0$ but $\partial\theta_1/\partial y$, which provides the driving force, is not zero. The disturbance quantities can be represented as $q_2(x, y) = \hat{q}(y)\mathrm{e}^{\mathrm{i}\delta x} + \text{c.c.}$, where q_2 stands for any of u_2, v_2, p_2, θ_2, and the system can be expressed in terms of $\hat{v}$ in the form

$$(\mathrm{D}^2 + \delta^2)^3\hat{v} = -\delta^2 2^{-9} Ra_p^2\alpha^{-3}\hat{v}, \tag{3.11}$$

where $\mathrm{D} = \mathrm{d}/\mathrm{d}y$. Equation (3.11) can be brought to the same form as found in classical RB convection by introducing Rayleigh number Ra based on the layer

thickness $2h$ as the length scale and the temperature jump between the edge of the boundary layer and the upper wall as the temperature scale. The relation between Ra_p and Ra can be readily developed as

$$Ra_p^2\alpha^{-3} = 2^5 Ra, \tag{3.12}$$

where the temperature gradient given by (2.19) has been used. The position of the critical curve shown in figure 6 justifies use of this temperature gradient. Rescaling (3.11) with $2h$ as the length scale and using (3.12) leads to

$$(\tilde{\mathrm{D}}^2 + \tilde{\delta}^2)^3 \hat{v} = -\tilde{\delta}^2 Ra\, \hat{v}, \tag{3.13}$$

where $Ra = 2^{-5}\alpha^{-3}Ra_p^2$ and tildes identify quantities scaled with the new length scale. It is known (Chandrasekhar 1961) that the most unstable eigenvalue of (3.13) corresponds to $Ra = 1708$ and $\tilde{\delta}_{cr} = 3.12$, which gives

$$Ra_{p,cr} \to 2^{5/2}1708^{1/2}\alpha^{1.5} = 233.8\alpha^{1.5}, \quad \delta_{cr} \to 1.56 \quad \text{as } \alpha \to \infty. \tag{3.14}$$

The asymptote given by (3.14) is in excellent agreement with the complete solution, as illustrated in figure 9(*a*). It may be concluded that the role of the primary convection in this limit is to set up a conduction layer with a vertical temperature gradient large enough to drive the instability. The resulting instability process is qualitatively similar to the Rayleigh–Bénard convection (Chandrasekhar 1961) and, thus, we shall refer to it as driven by the RB (Rayleigh–Bénard) mechanism. The motion due to instability is spread in the bulk of the fluid with the modifications due to the periodic heating confined to the bottom boundary layer.

The simplified model (3.11) can be improved by including modes $(-1, 1)$ in the basic-state velocity field, modes $(-1, 0, 1)$ in the mean temperature field and limiting the stability problem to modes $(-1, 0, 1)$. The corresponding explicit form of the disturbance equations can be easily written. This approach has been explored but not adopted, as it extends the validity of the asymptotic approximation to marginally smaller α at the expense of complex computations.

Reduction of the heating wavenumber to $\alpha = O(1)$ increases the magnitudes and significantly changes the form of the velocity and the temperature fields, as discussed in § 2. In order to assess the effects of these fields, the critical curve has been recomputed using different representations of the basic state. In case 1, information about the velocity field has been eliminated but the complete representation of the temperature field has been retained. Further simplification was made in case 2 where the representation of the temperature field had been reduced to modes $(-1, 0, 1)$ only, and in case 3 where this representation had been further reduced to mode 0 only. Results displayed in figure 11(*a*) demonstrate that mixing associated with the velocity field has a small stabilizing effect, the difference between the full temperature field and its representation using modes $(-1, 0, 1)$ is negligible and use of only mode 0 from the temperature field has a noticeably stabilizing effect. These results demonstrate that the dominant destabilizing effect is associated with the unstable mean temperature gradient (mode 0 in the temperature field), which is set up by the nonlinear interactions taking place in the convection zone, and by the x-modulation of the temperature field (modes -1 and 1). Modulations are responsible for a noticeable reduction of $Ra_{p,cr}$, as illustrated by the difference between curve 4 and curves 2 and 3 in figure 11(*a*), which can be attributed to parametric resonance. Curves 5 and 6 demonstrate that the conductive part of the temperature modulations is more important. Movement of the fluid does not contribute directly, but provides a mechanism for

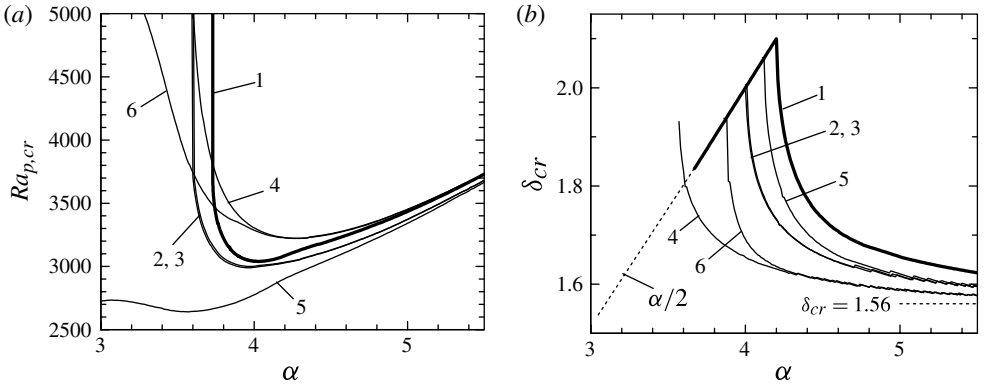

FIGURE 11. Variations of (*a*) the critical Rayleigh number $Ra_{p,cr}$ and (*b*) the critical wavenumber δ_{cr} as functions of α for different models of the basic state for the longitudinal rolls. Curve 1 (thick line) uses the complete representation of the flow and temperature fields, curve 2 neglects the velocity field while retaining the complete temperature field, curve 3 further reduces the temperature field to modes $(-1, 0, 1)$, curve 4 uses only mode 0 to represent the temperature field, curve 5 uses temperature modes $(-1, 0, 1)$ with modes $(-1, 1)$ retaining only the conductive component, while curve 6 follows curve 5 but with modes $(-1, 1)$ retaining only the convective component.

creation of the mean vertical temperature gradient. The role of parametric resonance has been further analysed by computing stability characteristics with the basic state represented only by the mean flow modulation using modes $(-1, 1)$, then by only the temperature modulations using modes $(-1, 1)$ and, finally, using both the velocity and the temperature field modulations. In all these cases no instability has been detected. It has been concluded that the modulation effects acting alone are unable to destabilize the longitudinal rolls within the range of Ra_p of interest.

The structure of the disturbance motion is a strong function of α (see figure 10). When $\alpha < \alpha_B = 4.2$, the external heating and the disturbance patterns are locked in according to the relation $\delta_{cr} = \alpha/2$. When $\alpha > \alpha_B$, the lock-in is broken and there is no obvious relation between the heating and the disturbance patterns. Variations of δ_{cr} for $\alpha \to \infty$ follow an asymptote $\delta_{cr} = 1.56 + 7.05\mathrm{e}^{-0.85\alpha}$, with the limit being the same as for classical RB convection (Chandrasekhar 1961). When α decreases below the lock-in value of $\alpha_B = 4.2$, the form of the critical curve (see figure 9*a*) shows a rapid flow stabilization and this suggests that the lock-in contributes to the rapid stabilization, in addition to the rearrangement of the primary temperature field discussed above.

It is known that occurrence of the lock-in is related to the spatial modulation of the basic state (Manor *et al.* 2008, 2009) and occurs as a result of parametric resonance. Modulation of convection is very strong when $\alpha = O(1)$ but weakens when α increases, and eventually the lock-in disappears. Results displayed in figure 11(*b*), which displays variations of δ_{cr} as a function of α for different models of the basic state, demonstrate that only modulation of the temperature field is relevant. The lock-in persists after elimination of the velocity field and reduction of the temperature representation to modes $(-1, 0, 1)$ only. Use of only mode 0 to represent the temperature field eliminates the lock-in. Elimination of the lock-in is not directly related to the appearance of the conductive zone, as results for H (see figure 7) clearly show that temperature modulation persists across the layer for $\alpha < 5$ while

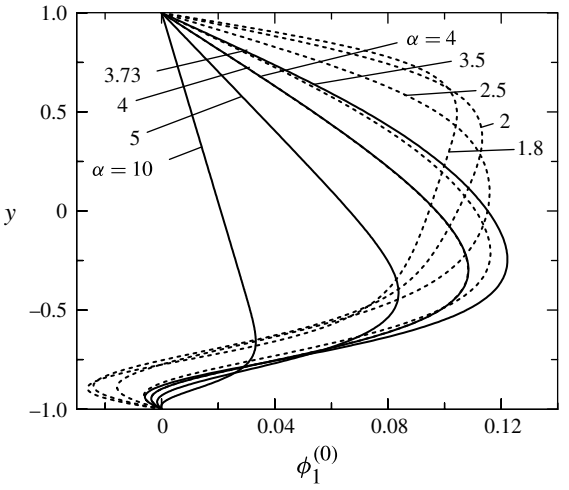

FIGURE 12. Distributions of $\phi_1^{(0)}$ at the onset for the longitudinal (solid lines) and oblique (dashed lines) rolls. For the longitudinal rolls, $(Ra_p, \alpha) = (7744.4, 10)$, (3435.2, 5), (3041.8, 4), (3663.4, 3.73). For the oblique rolls, $(Ra_p, \alpha) = (3035.7, 4)$, (2863.7, 3.5), (2505.7, 2.5), (5918.9, 2), (14030.3, 1.8).

the lock-in occurs only for $\alpha < \alpha_B = 4.2$. It may be concluded that the lock-in is caused by the x-modulation of the temperature field through parametric resonance primarily with the conductive component of the temperature field. This conclusion is also supported by the difference between the critical curve 4 and curves 2, 3, 5 and 6 in figure 11(a). Reduction of intensity of this modulation associated with an increase of α eliminates the resonance and breaks the lock-in. A precise determination of the break up conditions requires detailed analysis.

Figure 12 illustrates the evolution of the mean temperature at the onset. Reduction of α results in an increase of thickness of the zone with a stable mean vertical temperature gradient, and this weakens the RB mechanism. The instability can be maintained via an increase of the temperature gradient across the unstable zone, but this requires a rapid increase of $Ra_{p,cr}$.

Analysis of results presented in figures 9–12 shows that there are two mechanisms that contribute to the instability. In the case of large α, the instability is driven by the mean vertical temperature difference created by the primary convection (the RB mechanism). In the case of $\alpha = O(1)$, the RB mechanism is essential for the instability but the system response is strongly affected by parametric resonance. Conditions that separate the locked and unlocked zones (point B in figures 9–10) may be considered as representing a border between the zones where parametric resonance effects are relevant and where they can be ignored.

The pattern of disturbance motion changes considerably with α. In the locked-in state the pattern is rather simple, as illustrated in figure 13. The subharmonic relation between the primary convection and the disturbance pattern is clearly visible.

There are many possible patterns for the unlocked state as their forms are dictated by the dispersion relation $\delta_{cr} = \delta_{cr}(\alpha)$. It is convenient to view α as an externally imposed control parameter (heating pattern) and δ_{cr} as a measure of the system response. The dispersion relation is very simple for $\alpha \to \infty$ as, in this limit, $\delta_{cr} \to 1.56$; our discussion begins with this case. The numerical results show that

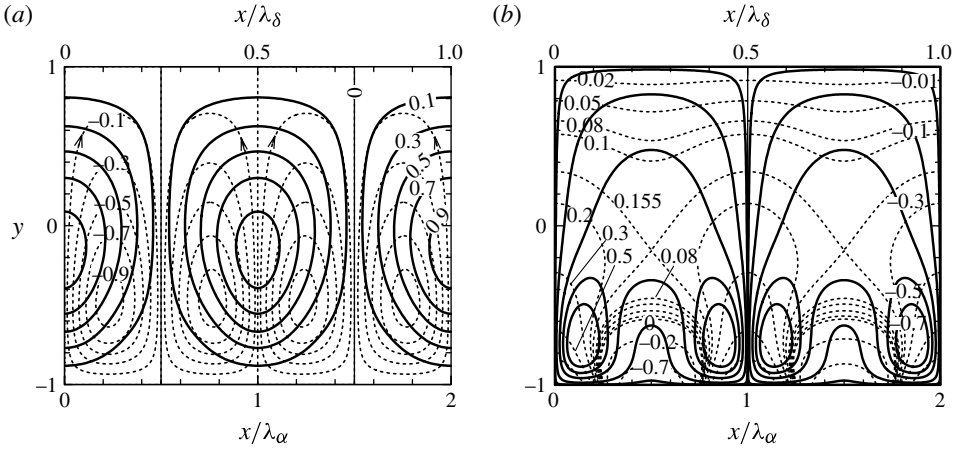

FIGURE 13. Disturbance streamlines (*a*) and isotherms (*b*) for $\alpha = 4.1$ at the onset of the longitudinal roll instability ($Ra_p = 3042.3$; letter L in figure 15). The primary and secondary flow quantities are represented using dashed and solid lines, respectively. The primary stream function and the temperature are normalized with their maxima ($\psi_{1,max} = 1.9091$, $\Theta_{1,max} = 2 * Pr$).

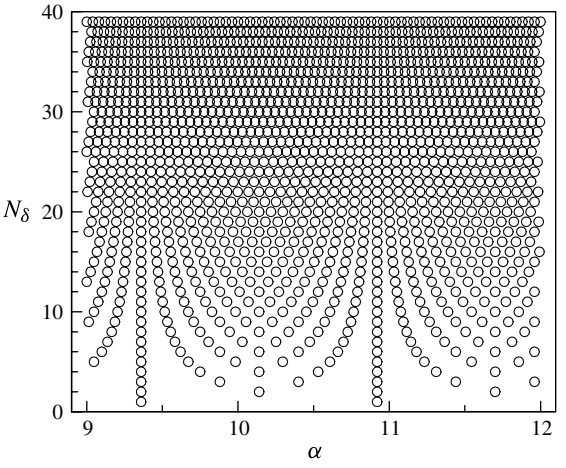

FIGURE 14. The possible *x*-periodic states of the system in the 'large-α' regime. The wavelength of the system is expressed in terms of the number of disturbance wavelengths N_δ.

the large-α limit is effectively reached when $\alpha > 9$. As α is arbitrary (but large) and $\delta_{cr} = 1.56$, the system exhibits commensurable (periodic) and non-commensurable (quasi-periodic) states. They can be categorized using the wavelength of the flow system expressed either in terms of the number of the disturbance wavelengths N_δ or in terms of the number of the heating wavelengths N_α. For each N_δ there is a discrete band of α able to produce this particular N_δ; simple analysis shows that all α corresponding to a given N_δ can be expressed as $\alpha = 1.56N_\alpha/N_\delta$. Results displayed in figure 14 illustrate such α or, alternatively, illustrate the possible periodic states for

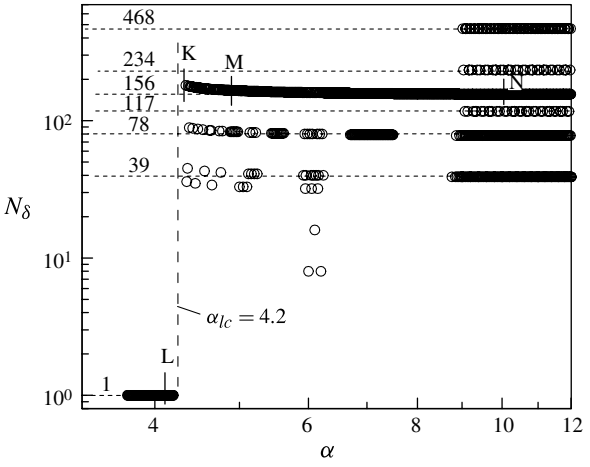

FIGURE 15. Variations of the wavelength of the disturbance flow structures for the longitudinal roll instability as a function of α at the onset measured using the number of disturbance wavelengths N_δ. Additional information about the structure of the unstable motion corresponding to conditions marked with letters K, M, N is displayed in figure 16, and for L in figure 13.

each α. This shows that the secondary convection has features of a frustrated system (Nixon *et al.* 2013) as multiple states are possible for each α.

Application of the heating with α between the lock-in value of $\alpha_B = 4.2$ and $\alpha \approx 9$ (the effective large-α limit) produces a number of intriguing flow structures. Commensurable states are illustrated in figure 15, where N_δ has been determined by searching for the lowest common denominator of α and δ_{cr} (Floryan 1997, 2003, 2005). The structures form bands in the (N_δ, α) plane that can be categorized by value of N_δ reached for $\alpha \to \infty$. These bands have been determined numerically, and searching for pairs (δ_{cr}, α) that correspond to the band of interest involves trial and error. Data presented in figure 15 have been determined by varying α with constant step sizes of $\Delta\alpha = 1/100$ and $\Delta\alpha = 1/12$. Only certain bands can be reached by such a process as the numerical evaluation of δ_{cr} is done with finite accuracy; δ_{cr} had been evaluated with an accuracy of four decimal points but only two decimal points were retained for evaluation of N_δ.

Changes in the structure of the disturbance velocity field are very similar for all bands subject to analysis ($N_\delta = 39, 78, 156, 256, 234$) and, thus, detailed results are given only for $N_\delta = 156$. The disturbance flow patterns are illustrated with the help of the disturbance stream function ψ_2 that is defined in the usual manner on the basis of u_2 and v_2. Variations of ψ_2 demonstrate the existence of a 'beating' pattern for α slightly above the lock-in (figure 16*a*), this pattern transitions to a 'wavy' pattern with increase of α (figure 16*b*), and eventually a 'large-α' pattern dominated by $\delta_{cr} = 1.56$ emerges (figure 16*c*). Streamlines for the 'beating' pattern (see figure 17) demonstrate that the disturbance field consists of rolls with almost identical topologies but with their strengths changing in a periodic manner along the x direction. One can easily identify zones with high and low motion intensities. Streamlines for the 'wavy' pattern displayed in figure 18 demonstrate that the disturbance flow field consists of pairs of rolls rotating in opposite directions with 'opposite' characteristics, i.e. at the beginning of each spatial cycle one roll is larger but has less intense motion and the other

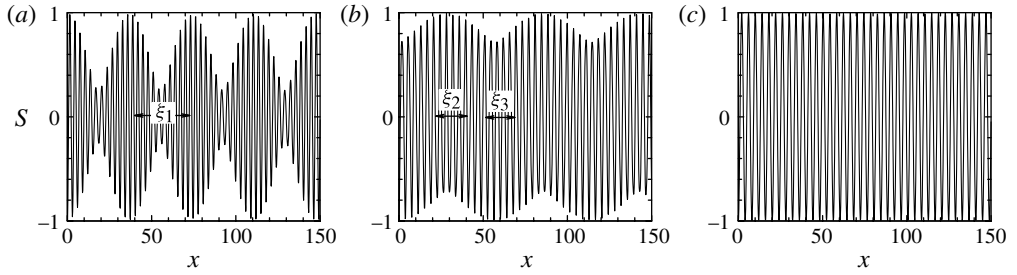

FIGURE 16. Variations of the disturbance stream function $S = \psi_2(x, 0)$ at $y = 0$ for the disturbance wavelength band $N_\delta = 156$. Results shown in (*a–c*) correspond to the onset conditions $(\alpha, \delta_{cr}, Ra_{p,cr}) = (4.21, 2.02, 3083)$, $(4.9, 1.67, 3389)$ and $(10.01, 1.56, 7749)$, respectively, and are marked with letters K, M, N in figure 15, respectively. The disturbance field in the x-interval labelled as ξ_1 in (*a*) is displayed in figure 17, and in intervals labelled as ξ_2 and ξ_3 in (*b*) are displayed in figure 18.

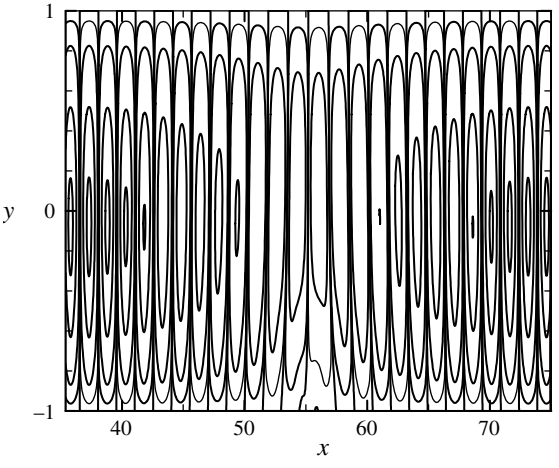

FIGURE 17. Disturbance flow field corresponding to the 'beating' pattern at the critical point $(\alpha, \delta_{cr}, Ra_{p,cr}) = (4.21, 2.02, 3083)$ for $N_\delta = 156$. The contour lines shown correspond to $\psi_2(x, y) = 0, 0.01, 0.1, 0.5, 0.7$ of its maximum. The range of x used for display is marked with symbol ξ_1 in figure 16(*a*).

one is smaller and has more intense motion. Their characters are reversed after half a cycle, i.e. the small roll expands and motion in its interior slows down while the larger roll contracts and motion in its interior intensifies. Patterns corresponding to transition zones between the 'beating', 'wavy' and 'large-α' patterns cannot be easily categorized and are not shown.

An insight into the patterns is provided by modulations of the phase illustrated using the local wavenumber δ_{local} determined on the basis of zeros of the disturbance stream function; δ_{local} is determined by distance between two subsequent zeros. Variations of δ_{local} illustrated in figure 19 demonstrate the existence of competition between the locked-in wavenumber $\delta_{cr} = \alpha/2$ and the 'large-α' wavenumber $\delta_{cr} = 1.56$. In the case of the 'beating' pattern (figure 16*a*, $\alpha = 4.21$), the system is still strongly influenced by the lock-in effect producing wide and flat maxima with $\delta_{local} \approx 2.08$ separated by narrow minima with $\delta_{local} \approx 1.8$ giving the appearance of a solitary phase modulation

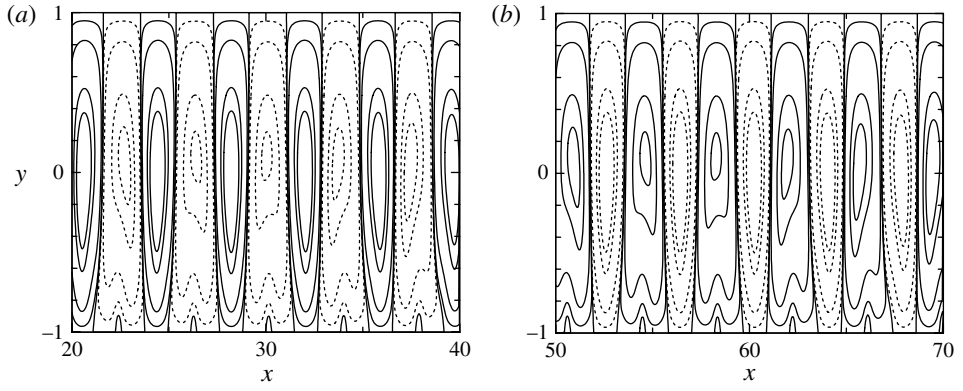

FIGURE 18. Disturbance flow field corresponding to the 'wavy' pattern at the critical point $(\alpha, \delta_{cr}, Ra_{p,cr}) = (4.9, 1.67, 3389)$ for $N_\delta = 156$. The contour lines shown correspond to $\psi_2(x, y) = 0, 0.01, 0.1, 0.5, 0.7$ of its maximum. Solid and dotted lines are used to identify rolls rotating in the opposite directions. Ranges of x displayed in (a,b) are marked in figure 16(b) by symbols ξ_2 and ξ_3, respectively.

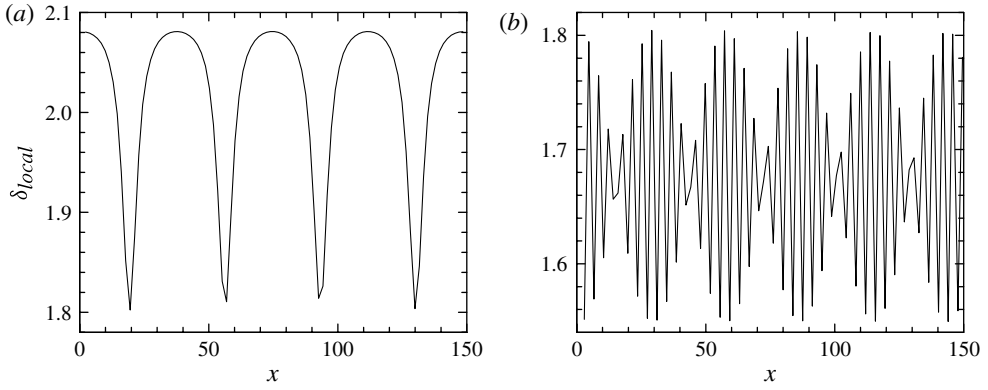

FIGURE 19. Solitary roll structure. Results displayed in (a,b) have been extracted from the data displayed in figure 16(a,b), respectively.

(see figure 19a). These solitons form a lattice that is parallel to the rolls. Solitons are known to mediate transition between the commensurate and non-commensurate patterns and have been observed in pattern-forming hydrodynamic instabilities (McCoy *et al.* 2008; Seiden *et al.* 2008; Lowe & Gollub 1985). The maxima of δ_{local} correlate with the areas of high intensity motion and the minima correspond to the zones of low intensity motion. In the case of the 'wavy' pattern (figure 16b, $\alpha = 4.9$), the two effects are at par, resulting in a continuous and rapid adjustment of δ_{local} between 1.56 and 1.8 (see figure 19b) that is repeated periodically in the x direction and forms a lattice. The minima of the amplitude of variations of δ_{local} correspond to zones where the rolls with the clockwise and anticlockwise rotations have similar intensity while the maxima identify regions with a preferred direction of rotation. In the large-α zone (figure 16c) δ_{local} overlaps with $\delta_{cr} = 1.56$ to within numerical accuracy.

Analysis of disturbance fields for disturbances belonging to bands $N_\delta = 78$ and 39 shows the existence of similar 'beating' and 'wavy' structures but with wavelengths

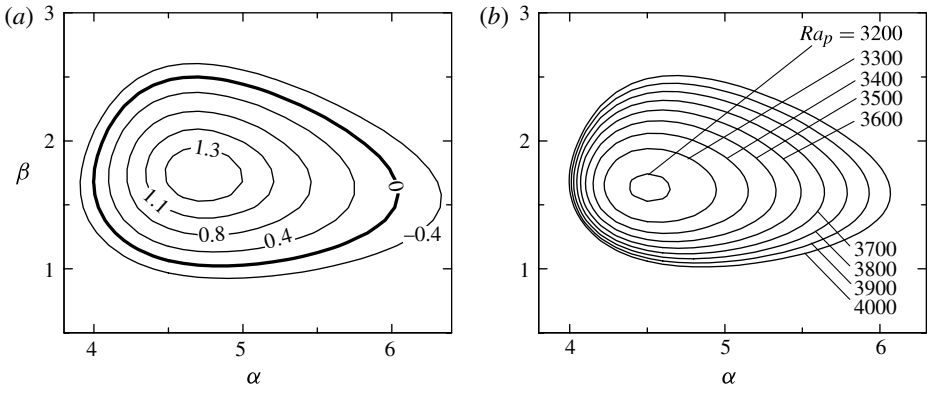

FIGURE 20. (*a*) Variations of the amplification rate $\mathrm{Im}(\sigma)$ of the transverse rolls for $Ra_p = 3980$ and (*b*) variations of the neutral stability conditions as a function of the heating wavenumber α and the transverse roll wavenumber β for fixed Ra_p.

and amplitudes different from those found for $N_\delta = 156$. This indicates that these patterns represent characteristic features of spatially modulated systems.

3.3.2. *Transverse rolls*

Transverse rolls are characterized by the wave vector $\boldsymbol{q} = (0, \beta)$, i.e. they have axes orthogonal to the axes of the primary rolls, and lead to the formation of a flow system with rectangular symmetries.

Figure 20(*a*) displays variations of the amplification rate of the transverse rolls as a function of α and the roll wavenumber β for a fixed Rayleigh number $Ra_p = 3980$. Figure 20(*b*) displays a set of neutral curves. A decrease of Ra_p results in reduction of the range of destabilizing heating patterns and reduction in the range of rolls' wavenumbers produced by the instability. The instability does not occur at all for $Ra_p < 3200$.

The critical stability conditions identified in the same manner as for the longitudinal rolls are displayed in figures 9–10. The minimum heating intensity required to induce this instability corresponds to $Ra_{p,min} = Ra_F = 3188.6$ (point F in figure 9) but the instability will occur only if the heating pattern corresponds to $\alpha_{min} = \alpha_F = 4.51$. An increase of Ra_p above 3188.6 increases the range of unstable α. The critical curve rises steeply when α is reduced below $\alpha_F = 4.51$, which indicates the stabilizing effect of strong convection, as in the case of longitudinal rolls. An increase of α above $\alpha_F = 4.51$ results in a gradual increase of $Ra_{p,cr}$, which eventually follows the same asymptote as for the longitudinal rolls, i.e. $Ra_{p,cr} \to 2^{5/2}1708^{1/2}\alpha^{1.5}$ as $\alpha \to \infty$.

The mechanism responsible for generation of transverse rolls for large α is the same as in the case of longitudinal rolls, i.e. it is the RB mechanism. Reduction of α alters the system dynamics because of increase in the strength of spatial modulations, as documented in § 2. This dynamics is a bit different from the one observed for the longitudinal rolls as both the velocity and the temperature modulations play an essential role in the resonance. In order to document this mechanism, the critical curve has been recomputed using different representations of the basic state. Tests with mode zero eliminated from the temperature field showed no instability and this demonstrates the dominant role of the RB mechanism. Complete elimination of the velocity field results in the reduction of $Ra_{p,cr}$ and expansion of the instability into smaller α (see curve 2 in figure 21), and thus demonstrates the stabilizing role of velocity. Use of

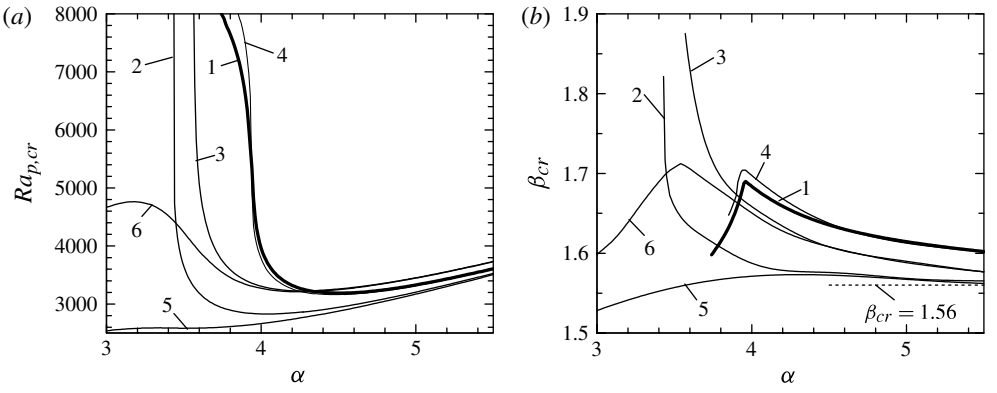

FIGURE 21. Variations of the critical Rayleigh number $Ra_{p,cr}$ and the critical wavenumber β_{cr} as functions of α for different models of the basic state for the transverse rolls. Curve 1 (thick line) uses the complete representation of the flow and temperature fields, curve 2 completely eliminates the velocity field and uses modes $(-1, 0, 1)$ to represent the temperature field, curve 3 uses modes $(-1, 1)$ to represent the velocity field and mode (0) to represent the temperature field, curve 4 uses modes $(-1, 1)$ to represent the velocity field and modes $(-1, 0, 1)$ to represent the temperature field, curve 5 uses the same conditions as curve 4 but modes $(-1, 1)$ in the temperature field contain only conductive contributions, while in curve 6 these modes contain only convective contributions.

either the full representation of the temperature field or just modes $(-1, 0, 1)$ results in nearly identical critical curves, so only the latter is shown. Further reduction of the temperature field to just mode (0) increases $Ra_{p,cr}$ by $\sim$500 and reduces the range of unstable α, but the qualitative character of system response remains the same (the corresponding critical curve is not shown). Use of velocity modulations represented by modes $(-1, 1)$ and only mode (0) in the temperature field results in considerable stabilization, but the qualitative character of system response still remains the same (see curve 3 in figure 21). Use of both the velocity modulations (modes $-1, 1$) and the temperature modulations (modes $-1, 0, 1$) changes the character of the system response, as the characteristic, abrupt change in the character of β_{cr} variations around $\alpha = 3.95$ is now reproduced. The corresponding critical curve (curve 4 in figure 21) very closely matches the actual curve (curve 1 in figure 21). It can be concluded that the basic state velocity stabilizes the system while the basic state temperature modulations destabilize it and expand the range of α that can produce instability. Comparison of curve 5, obtained in the same manner as curve 4 but with the temperature field limited to conductive contributions, and curve 6, obtained with the temperature field limited to convective contributions, demonstrates the essential role of the former.

The structure of the disturbance motion is also a strong function of α (see figure 10). Categorization of these structures is simple as they are uniquely determined by β_{cr}. One can identify two intervals with qualitatively different forms of variations of β_{cr}, with a transition taking place at $\alpha_D = 3.95$ where β_{cr} reaches the maximum of $\beta_{cr} = \beta_D = 1.69$ (point D in figure 10). The critical curve has a continuous derivative at this point; this is distinct from the similar curve in figure 11(*b*) which has a cusp at its maximum point. No characteristic relation can be found between β_{cr} and α in either of these intervals. When α decreases below $\alpha_D = 3.95$, β_{cr} quickly decreases and the flow is rapidly stabilized. When α increases above $\alpha_D = 3.95$, β_{cr} slowly decreases

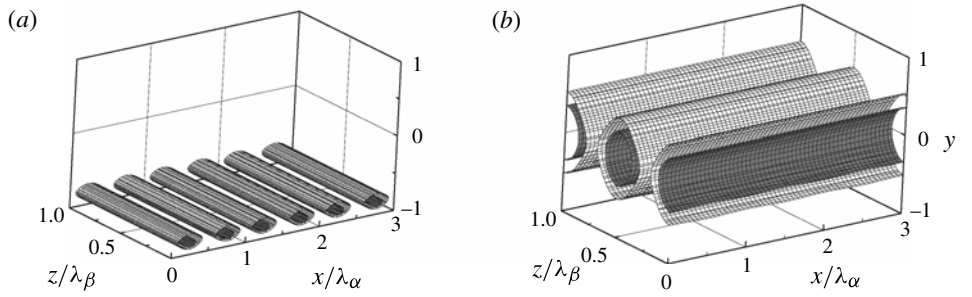

FIGURE 22. Flow structures created by (*a*) the primary convection and (*b*) the secondary convection in the form of transverse rolls generated by heating with the wavenumber $\alpha = 10$ at the onset ($Ra_{p,cr} = 7667.4$, $\beta_{cr} = 1.56$). Iso-surfaces with $\vartheta = 0.1, 0.5$ (see (3.15)) and $\vartheta = 0.2, 0.7$ are displayed in (*a,b*), respectively.

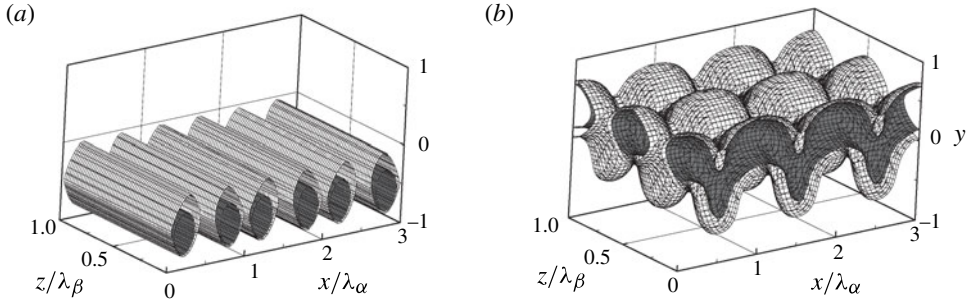

FIGURE 23. The same quantities as in figure 22 but for $\alpha = 3.95$, $Ra_{p,cr} = 4823.9$, $\beta_{cr} = 1.69$. Iso-surfaces for $\vartheta = 0.1, 0.3$ for the primary and the secondary convections are displayed in (*a,b*), respectively.

and approaches the limiting value $\beta_{cr} = 1.56$ for $\alpha \to \infty$, which is the same as for the longitudinal-roll instability.

Variations of topologies of the disturbance velocity fields as a function of α at the onset are illustrated in figures 22–24 using the second invariant of the velocity gradient tensor ϑ (Dubief & Delcayre 2000) defined as

$$\vartheta = \tfrac{1}{2}(\Phi_{ij}\Phi_{ij} - \varpi_{ij}\varpi_{ij}), \tag{3.15}$$

where $\Phi_{ij} = (u_{i,j} - u_{j,i})/2$, $\varpi_{ij} = (u_{i,j} + u_{j,i})/2$. The disturbance velocity field has been normalized with condition $\max(g_{2u}^{(0)}) = 1$ for display purposes. The same figures display topologies of the primary velocity field for comparison purposes. When α is large, the primary convection at the onset is concentrated very close to the heated wall (figure 22*a*) and is unable to modulate the disturbance velocity field which is centred in the middle of the layer (figure 22*b*). Reduction of α leads to a rapid increase of the strength of the primary convection and its upward expansion as illustrated in figure 23(*a*). The secondary rolls become distorted by strong upward currents above the hot spots and downward currents above the cold spots (figure 23*b*). Further reduction of α continues the same process, i.e. the primary convection becomes still stronger (figure 24*a*) and the upward and downward currents produce more extreme deformation of the secondary rolls. These rolls contract and deform in locations where

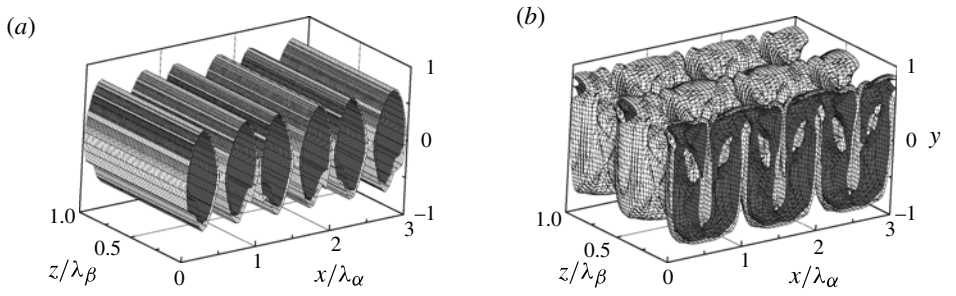

FIGURE 24. The same quantities as in figure 22 but for $\alpha = 2.47$, $Ra_{p,cr} = 24166.5$, $\beta_{cr} = 1.35$. Iso-surfaces for $\vartheta = 0.2, 0.45$ for the primary convection and for $\vartheta = 0.12, 0.3$ for the secondary convection are displayed in (*a,b*), respectively.

they are pushed against the walls, cores of the rolls expand significantly in the zones where vertical motion is minimal but, nevertheless, the rolls maintain continuity and do not break up into discrete cells (figure 24*b*). More intense heating is required to sustain such highly distorted rolls, leading to rapid increase of $Ra_{p,cr}$, as shown in figure 9. The importance of convection currents, which are responsible for the roll distortion, and the resulting stabilization are clearly identified in the results presented in figure 21.

Comparison of the two instabilities (see figures 9–10) shows that the transverse rolls dominate over the longitudinal rolls for $\alpha < \alpha_C = 3.72$, there is a range of alpha ($\alpha_C = 3.72 < \alpha < \alpha_E = 4.46$) where the longitudinal rolls dominate, and the transverse rolls dominate again for $\alpha > \alpha_E = 4.46$. Both types of rolls may emerge for $\alpha = 3.72, 4.46$ and both have the same asymptotes for $\alpha \to \infty$ with $Ra_{p,cr}$ for the transverse rolls being always below $Ra_{p,cr}$ for the longitudinal rolls.

The transverse roll instability is driven in the 'large-α' zone by the RB mechanism associated with the formation of the conduction layer (see figure 7). When α decreases to $O(1)$, the zone with the unstable mean temperature gradient is reduced to a fraction of the layer thickness (see figure 12), the temperature field exhibits strong horizontal modulations, and rolls become exposed to strong x-periodic convection currents. As a result, parametric resonance builds up and is eventually strong enough to cause a qualitative change in the character of variations of β_{cr} at $\alpha_D = 3.95$ (see figure 10). Since this transition occurs for large Ra_p, its details are not presented. It can be concluded that the transverse rolls are driven by the mean vertical temperature gradient, but the system response is affected by the temperature and velocity modulations associated with the primary convection currents.

3.3.3. *Oblique rolls*

Instability mechanisms responsible for the onset of longitudinal and transverse rolls have been described in the previous sections. They include the RB mechanism, which is dominant for large α, and parametric resonance, which becomes important at $\alpha = (1)$ and leads to the phase lock-in. Velocity modulations play a minimal role in the onset of the longitudinal rolls but have a significant effect on the onset of the transverse rolls. We shall now turn our attention to the most general case, i.e. oblique rolls, where the system exhibits rhombic symmetry. Such rolls are characterized by the wave vector $\boldsymbol{q} = (\delta, \pm\beta)$ with magnitude $|\boldsymbol{q}| = (\beta^2 + \delta^2)^{1/2}$ and inclination angle $\eta = \pm\tan^{-1}(\beta/\delta)$. Longitudinal rolls correspond to $\eta = 0°$ and transverse rolls to $\eta = 90°$.

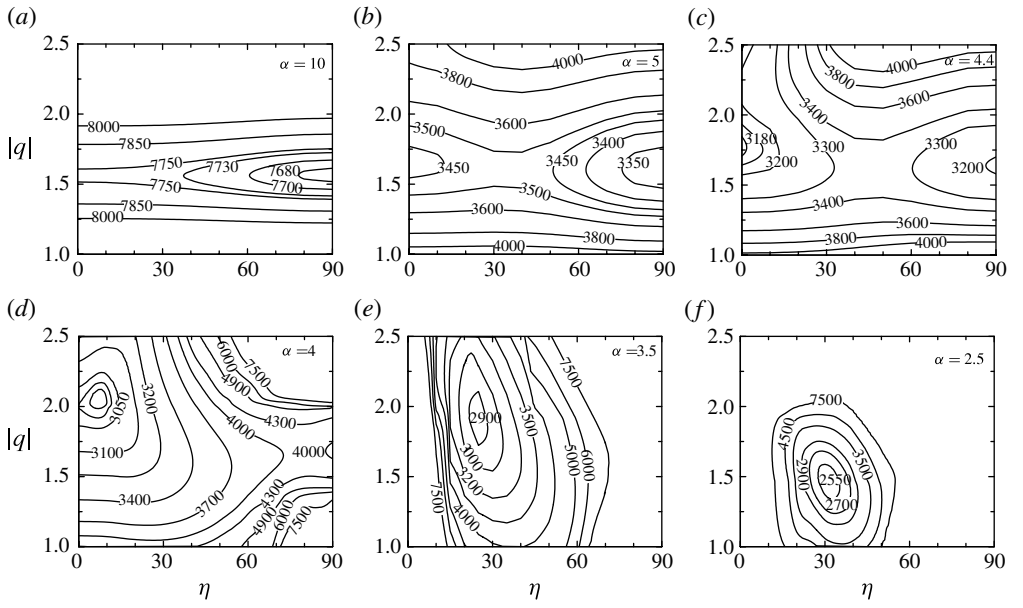

FIGURE 25. Neutral surfaces in the space formed by the roll wavenumber $|\boldsymbol{q}|$, the roll inclination angle η and the Rayleigh number Ra_p.

Figure 25(*a*) displays the neutral surface in the $(Ra_p, |q|, \eta)$ space for $\alpha = 10$ (the 'large-α' zone). The minimum of Ra_p corresponds to $|q| = 1.56$ and $\eta = 90°$ (transverse rolls). This minimum is flat in the η direction with the change of Ra_p between $\eta = 90°$ and $\eta = 0°$ being ∼130, which demonstrates a weak preference for transverse rolls. It has been shown in the previous sections that the instability for large α is qualitatively similar to RB convection but the residual presence of the x-modulation gives a preference to transverse rolls. The minimum is steep in the $|\boldsymbol{q}|$ direction, showing a strong preference for the size of the rolls. The system response is qualitatively similar to RB convection, with short-wavelength, symmetry-breaking spatial temperature modulations imposed at the lower wall (Freund *et al.* 2011).

Reduction of the heating wavenumber to $\alpha = 5$ (figure 25*b*) demonstrates the emergence of two distinct local minima, one centred at $\eta = 0°$, $|\boldsymbol{q}| \approx 1.7$ and the other at $\eta = 90°$, $|\boldsymbol{q}| \approx 1.6$. Transverse rolls with $|\boldsymbol{q}|$ slightly higher than in the 'large-α' zone continue to play the critical role. Gradients in the η and $|\boldsymbol{q}|$ directions show a weak preference for the orientation of the rolls but a strong preference for the size. Further reduction of the heating wavenumber to $\alpha = 4.4$ maintains distinct minima, but leads to a reversal of their roles, with the minimum at $\eta = 0°$ becoming the global minimum and the longitudinal rolls playing the critical role (see figure 25*c*). The parametric resonance is still too weak to produce the lock-in effect.

Heating with $\alpha = 4$ (figure 25*d*) corresponds to conditions when the longitudinal rolls become locked in with the primary rolls and stop playing the critical role. The global minimum moves to $\eta \approx 8°$ and the roll size decreases to $|\boldsymbol{q}| \approx 2.1$. Heating with $\alpha = 3.5$ produces only a single minimum with $\eta \approx 28°$ and $|\boldsymbol{q}| \approx 1.8$ (figure 25*e*). The minimum of $Ra_{p,cr}$ is reached at $\alpha = 2.69$ (see figure 9) and its further reduction leads to a rapid increase of $Ra_{p,cr}$, a small increase of the inclination angle η and a large increase of the roll size (see figure 25*f*).

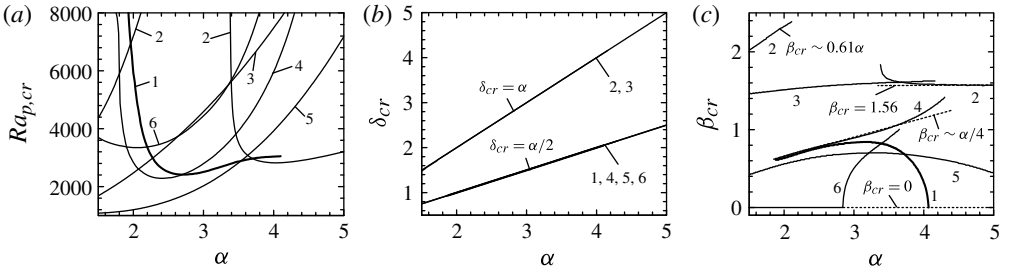

FIGURE 26. Variations of the critical Rayleigh number $Ra_{p,cr}$ (a) and the critical wavenumbers δ_{cr} (b) and β_{cr} (c) as functions of α for different models of the basic state for the oblique rolls. Curve 1 (thick line) uses the complete representation of the flow and temperature fields, curve 2 eliminates the velocity field and uses the complete temperature field, curve 3 eliminates the velocity field and uses the temperature field represented by modes $(-1, 1)$ only, curve 4 uses the complete velocity field and the temperature field represented by modes $(-1, 1)$ only, curve 5 uses the same conditions as curve 4 but modes $(-1, 1)$ in the temperature field contain only the conductive contributions (see (2.2)), while in curve 6 these modes contain only the convective contributions.

Variations of the global and local minima as functions of α are illustrated in figure 9 and identify the overall critical stability conditions. The transverse rolls play the critical role for $\alpha > \alpha_E = 4.46$ and the system has rectangular symmetry. At $\alpha = \alpha_E = 4.46$ the longitudinal and the transverse rolls have the same critical Ra_p. The longitudinal rolls dominate for $\alpha_E = 4.46 > \alpha > \alpha_A = 4.03$, producing a system with translational symmetry. The curve that eventually becomes the critical curve for the oblique rolls originates at $\alpha_H = 4.07$. For these conditions a separate local minimum corresponding to oblique rolls forms in the $(\eta, |\boldsymbol{q}|)$ plane; this minimum is similar to the minimum shown in figure 25(d) but it coexists with the global minimum at $\eta = 0°$. The local minimum of Ra_p moves away from the axis $\eta = 0°$ and decreases as α decreases. The minima for the oblique and longitudinal rolls attain the same levels at $\alpha_A = 4.03$ where the two structures coexist. The local minimum corresponding to the oblique rolls becomes the global minimum for $\alpha < \alpha_A = 4.03$ and the system acquires rhombic symmetry.

The continuous change in the disturbance topology summarized above due to decrease of α corresponds to an increase in the relative strength of spatial modulations and a decrease of the strength of the RB mechanism. As a result, the oblique rolls become the most 'efficient' at sufficiently small α, the translation symmetry is broken and replaced by the rhombic symmetry, the unstable zone expands to smaller α and the critical Rayleigh number drops to $Ra_{p,cr} = Ra_G = 2411.2$ at $\alpha = \alpha_G = 2.69$. Reduction of α below 2.69 leads to a rapid stabilization, which is remarkable as no roll may appear for $\alpha < 1.6$ for Ra_p of interest.

The oblique rolls represent a very interesting feature of system dynamics as they are generated by the spatial parametric resonance. These rolls play a critical role for $\alpha < 4.03$, and under such conditions the basic state exhibits strong spatial modulations (see § 2). The dominant role of spatial resonance for small α can be demonstrated by computing critical curves with various representations of the basic state. Curve 1 in figure 26 has been obtained with its complete representation and exhibits lock-in in the form $\delta_{cr} = \alpha/2$ in the x direction and lack of regular variations of β_{cr}, with β_{cr} approaching lock-in in the form $\beta_{cr} \sim \alpha/4$ for sufficiently small α.

Complete elimination of the temperature results in system stabilization and leads to an obvious conclusion that the velocity field cannot produce instability by itself. Complete elimination of the velocity shows that the instability can be driven just by the temperature field (see curve 2 in figure 26). In this case the critical curve is split into two branches, the left one showing destabilization for $\alpha < 2.2$ and the right one showing destabilization for $\alpha > 3.4$. Comparison of curves 1 and 2 demonstrates a dual role of velocity, i.e. contribution to destabilization for $2.2 < \alpha < 3.4$ but stabilization for $\alpha < 2.2$. The left branch exhibits lock-in in the form $\delta_{cr} = \alpha$ and $\beta_{cr} \sim 0.61\alpha$; the right one retains the same lock-in for δ_{cr} but β_{cr} does not exhibit any regularity except when approaching limit $\beta_{cr} \to 1.56$ for large α. Further elimination of the mean temperature gradient from the temperature field (elimination of the RB mechanism) leads to destabilization for small α but stabilization for larger α (curve 3 in figure 26). This demonstrates the stabilizing role of the RB mechanism for small α but its destabilizing role for large α, and the destabilizing role of temperature modulations for small α. The lock-in for the x direction remains the same but $\beta_{cr} \approx 1.56$ in the whole range of α of interest. Use of the complete velocity field and temperature represented only by modes $(-1, 1)$ results in a critical curve that approximately matches the complete curve on the small-α side but shows stabilization on the large-α side (curve 4 in figure 26). This provides a basis for the conclusion that the oblique rolls are driven by the parametric resonance associated with the temperature modulations and significantly modified by the velocity modulations. The RB mechanism remains active but its strength weakens and changes from destabilizing to stabilizing as α decreases. This changeover can also be deduced from the form of the mean temperature distributions at the onset, displayed in figure 12, which demonstrates its existence in a stable mean temperature gradient over the majority of the layer height, and the increase of the size of this zone as α is reduced. The x-lock-in is the same as in the complete problem and the z-lock-in acquires the same limit for small α. The origin of the most important part of the thermal modulations is deduced by comparing curve 5 produced with thermal modulations coming from the conductive effects only (see (2.2)) with curve 6 produced with thermal modulations produced by the convective effects only. The dominant role of the conduction modulations and increase of their importance for smaller α are clearly visible.

Oblique structures are rarely observed in pattern-forming systems. Seiden *et al.* (2008) and McCoy *et al.* (2008) observed them in RB convection where patterns emerge with a well-defined wave vector by spontaneous symmetry-breaking bifurcation from an initial homogeneous state; addition of a one-dimensional spatially periodic forcing leads to a variety of new patterns, typically with rhombic symmetry. The stability of forced rolls in an RB system near the critical conditions and with temperature modulations has been investigated by Vozovoi & Nepomnyashchy (1974) and Pal & Kelly (1979), who pointed out the importance of oblique destabilizing modes. Smith & Davis (1983) identified oblique hydrothermal waves as critical in a liquid layer exposed to thermocapillary effects. Lyubimov & Shklyaev (2002) described transverse structures in a two-layer system with a deformable interface in a gravity field. Manor *et al.* (2008, 2009) considered a model problem that produces striped patterns when unforced, but forcing with a wavenumber mismatched with the pattern wavenumber results in a pattern locked in with forcing which, at the same time, develops a wave vector component perpendicular to the forcing direction and forms rhombic and oblique patterns. The current problem is different from those discussed above as the initial state is not homogeneous but is formed by periodic forcing. The

system nevertheless develops a wave vector component in the direction perpendicular to the forcing direction for a certain range of the forcing wavenumbers.

The flow topology associated with a single oblique roll at the onset is very similar to the transverse roll shown in figure 24(*b*). Since oblique rolls appear in pairs with the wave vectors $\boldsymbol{q}_{1,2} = (\delta_{cr}, \pm\beta_{cr})$, the secondary convection takes the form of finite cells of rhombic shape. The x/z aspect ratio of such cells is dictated by the fixed lock-in in the x direction and changes of β_{cr} illustrated in figures 10 and 26. As α decreases from $\alpha_H = 4.07$ down to $\alpha \approx 3$, β_{cr} increases rapidly from 0 to $\sim$0.8, resulting in a rapid rotation of the critical roll from $\eta = 0^\circ$ to $\sim 30^\circ$, an increase of its wavelength (the wavenumber changes from $|\boldsymbol{q}| = 2.035$ to 1.7) and an increase of the aspect ratio from 0 to 0.27. Further decrease of α marginally increases roll inclination; at the same time the roll size increases substantially as its wavenumber approaches asymptote in the form $|\boldsymbol{q}| \approx 0.56\alpha$ and the cell aspect ratio approaches 0.5.

4. Summary

Natural, buoyancy-driven convection of a Boussinesq fluid with Prandtl number $Pr = 0.71$ contained between two infinite horizontal walls has been analysed. The bottom wall is subject to a periodic heating in the x direction, the mean temperatures of the two walls are identical and the gravity vector is directed across the fluid layer. The spatial pattern and the intensity of the heating are expressed in terms of the heating wavenumber α and a Rayleigh number Ra_p based on the amplitude of temperature variations, respectively.

The primary response of the system consists of convection in the form of rolls whose orientation is determined by the heating wave vector $(\alpha, 0)$ and whose structure is dictated by the particular values of Ra_p and α. Heating with small and moderate α results in convection spreading throughout the bulk of the fluid. For a sufficiently large α convection is confined to a thin zone adjacent to the lower wall with a uniform conductive layer, with temperature independent of the x direction forming above. The strength of the convection changes in proportion to Ra_p/α^3 under such conditions. Sufficient increase of Ra_p causes convection to expand up into the bulk of the fluid. The nonlinear interactions give rise to the mean vertical temperature gradient that drives the net heat transfer between the two walls, with the heat flow being larger for smaller α and decreasing in proportion to α^{-3} when α increases.

Linear stability of the primary convection has been considered and conditions leading to the emergence of secondary convection have been identified. Depending on α, the secondary convection may take the form of either longitudinal, transverse, or oblique rolls. The longitudinal rolls are parallel to the primary rolls and the transverse rolls are orthogonal to the primary rolls, and both of them result in striped patterns. The oblique rolls lead to the formation of convection cells with rhombic patterns, with aspect ratio dictated by the roll inclination angle. This angle may change from 0 to 30° depending on α within the range of Ra_p of interest. Rapid stabilization and elimination of rolls is observed when the heating wavenumber is reduced below $\alpha \approx 2.2$ with no instability found for $\alpha < 1.6$ in the range of Ra_p considered.

Two mechanisms of instability at the onset have been identified. The first mechanism dominates in the case of large α, where the instability is driven by the mean vertical temperature gradient created by the primary convection, with the magnitude of the critical disturbance wave vector approaching the limiting value of 1.56 regardless of the roll orientation. Since rolls in this limit show a weak preference for the transverse orientation and the fluid response is similar to that found

in the case of a uniformly heated wall, this mechanism is referred to as the RB (Rayleigh–Bénard) mechanism. The strength of the second mechanism, the parametric resonance mechanism, gradually increases as α decreases and eventually dominates the system response. This response is characterized by a disturbance pattern with the x-component of the disturbance wave vector locked in with the heating wave vector according to the relation $\delta_{cr} = \alpha/2$ and the appearance of the disturbance wave vector component in the direction perpendicular to the heating wave vector. In the above, δ_{cr} denotes the component of the disturbance wave vector which is parallel to the heating wave vector. The RB mechanism may play a stabilizing role under such conditions. Modulations of both the primary temperature and the velocity fields are essential in the formation of the system response.

Competition between the two mechanisms results in three preferred disturbance patterns at the onset. The first pattern results from the dominance of the RB mechanism and leads to the formation of striped patterns orthogonal to the primary rolls. The second pattern results from a balance between the parametric resonance and the RB mechanism, and results in the formation of a striped pattern parallel to the primary rolls. The third pattern results from dominance of the parametric resonance, is produced by the phase lock-in between the x-components of the disturbance and the heating wave vectors and the appearance of the z-component of the disturbance wave vector, and leads to the formation of rhombic patterns.

The presented results demonstrate that the heating wavenumber α can be used as the pattern control parameter and its judicious selection provides a means for creation of a large range of flow responses.

Acknowledgement

This work was carried out with the support of NSERC of Canada.

Appendix

Assume a solution of (2.4) of the form

$$(u_1, v_1, p_1, \theta_1) = \varepsilon(U_1, V_1, P_1, \Theta_1) + \varepsilon^2(U_2, V_2, P_2, \Theta_2) + O(\varepsilon^3), \tag{A 1}$$

where ε is a small parameter measuring the strength of convection. Substitution of (A 1) into (2.4) and retention of the leading-order terms results in

$$\left.\begin{aligned} &\frac{\partial^2 U_1}{\partial x^2} + \frac{\partial^2 U_1}{\partial y^2} - \frac{\partial P_1}{\partial x} = 0, \quad \frac{\partial^2 V_1}{\partial x^2} + \frac{\partial^2 V_1}{\partial y^2} - \frac{\partial P_1}{\partial y} = -Ra_p \Theta_1 - Ra_p Pr^{-1}\hat{\theta}_0, \\ &\frac{\partial U_1}{\partial x} + \frac{\partial V_1}{\partial y} = 0, \quad \nabla^2 \Theta_1 = 0, \end{aligned}\right\} \tag{A 2}$$

where $\hat{\theta}_0 = \theta_0/\varepsilon = O(1)$. The above system needs to be supplemented by the homogeneous boundary conditions. Since Θ_1 is zero, a stream function in the form $\varepsilon\psi(x, y) = \alpha Ra_p Pr^{-1} F(y)\sin(\alpha x)$ can be introduced, where F is determined by solution of the problem

$$\mathrm{D}^4 F - 2\alpha^2 \mathrm{D}^2 F + \alpha^4 F = -\theta_c, \quad F(\pm 1) = \mathrm{D}F(\pm 1) = 0, \tag{A 3}$$

where θ_c is defined by (2.3). An analytical solution of (A 3) can be determined but is not presented, as it is excessively long and is not required for further discussion. It is sufficient to note that $\varepsilon U_1 = \alpha Ra_p Pr^{-1} \mathrm{D}F(y)\sin(\alpha x)$ and $\varepsilon V_1 = -\alpha^2 Ra_p Pr^{-1} F(y)\cos(\alpha x)$.

Energy equation of $O(\varepsilon^2)$ has the form

$$\frac{\partial^2 \Theta_2}{\partial x^2} + \frac{\partial^2 \Theta_2}{\partial y^2} = U_1 \frac{\partial \hat{\theta}_0}{\partial x} + V_1 \frac{\partial \hat{\theta}_0}{\partial y}, \tag{A 4}$$

and can be rearranged into

$$\frac{\partial^2 (\varepsilon^2 \Theta_2)}{\partial x^2} + \frac{\partial^2 (\varepsilon^2 \Theta_2)}{\partial y^2} = -0.5\alpha^2 Ra_p Pr^{-1} \mathrm{D}(F\theta_c) - 0.5\alpha^2 Ra_p Pr^{-1}(-\theta_c \mathrm{D}F + F\mathrm{D}\theta_c)\cos(2\alpha). \tag{A 5}$$

The solution of the aperiodic part has the form

$$\varepsilon^2 \Theta_2 = -0.5\alpha^2 Ra_p Pr^{-1} \int_{-1}^{y} F\theta_c \,\mathrm{d}y - 0.25\alpha^2 Ra_p Pr^{-1}(y+1) \int_{-1}^{1} F\theta_c \,\mathrm{d}y, \tag{A 6}$$

i.e. it contains components with both linear and highly complex y-dependence. It is shown in the text that the 'complex' component becomes confined to a boundary layer attached to the lower wall when $\alpha \to \infty$ and the linear component dominates outside the boundary layer. The net heat transport between the walls is driven by the linear component with the Nusselt number determined to be of the form

$$Nu = -0.25\alpha^2 Ra_p \int_{-1}^{1} F\theta_c \,\mathrm{d}y. \tag{A 7}$$

The above results demonstrate that both the strength of the convective motion and the Nusselt number initially increase in proportion to Ra_p. There is no heat flow in the absence of convection ($F = 0$).

REFERENCES

BELTRAME, P., KNOBLOCH, E., HÄNGGI, P. & THIELE, U. 2011 Rayleigh and depinning instabilities of forced liquid ridges on heterogeneous substrates. *Phys. Rev.* E **83**, 016305.

BLOCH, F. 1928 Über die Quantenmechanik der Elektronen in Kristallgittern. *Z. Physik* **52**, 555–600.

BODENSCHATZ, E., PESCH, W. & AHLERS, G. 2000 Recent developments in Rayleigh–Bénard convection. *Annu. Rev. Fluid Mech.* **32**, 709–778.

CHANDRASEKHAR, S. 1961 *Hydrodynamic and Hydromagnetic Stability*. Oxford University Press.

CLEVER, R. M. & BUSSE, F. H. 1974 Transition to time-dependent convection. *J. Fluid Mech.* **65**, 625–645.

CODDINGTON, E. A. & LEVINSON, N. 1965 *Theory of Ordinary Differential Equations*. McGraw-Hill.

DUBIEF, Y. & DELCAYRE, F. 2000 On coherent-vortex identification in turbulence. *J. Turbul.* **1**, 011.

FLORYAN, J. M. 1997 Stability of wall bounded shear layers in the presence of simulated distributed surface roughness. *J. Fluid Mech.* **335**, 29–55.

FLORYAN, J. M. 2003 Vortex instability in a diverging–converging channel. *J. Fluid Mech.* **482**, 17–50.

FLORYAN, J. M 2005 Two-dimensional instability of flow in a rough channel. *Phys. Fluids* **17**, 044101.

FLORYAN, J. M. 2012 Thermo-super-hydrophobic effect. *Bull. Am. Phys. Soc.* **57** (1) X50.00015.

FREUND, G., PESCH, W. & ZIMMERMANN, W. 2011 Rayleigh–Bénard convection in the presence of spatial temperature modulations. *J. Fluid Mech.* **673**, 318–348.

HOSSAIN, M. Z. & FLORYAN, J. M. 2013 Heat transfer due to natural convection in a periodically heated slot. *ASME J. Heat Transfer* **135**, 022503.

HOSSAIN, M. Z., FLORYAN, D. & FLORYAN, J. M. 2012 Drag reduction due to spatial thermal modulations. *J. Fluid Mech.* **713**, 398–419.

KELLY, R. E. & PAL, D. 1978 Thermal convection with spatially periodic boundary conditions: resonant wavelength excitation. *J. Fluid Mech.* **86**, 433–456.

KIERZENKA, J. & SHAMPINE, L. F. 2001 A BVP solver based on residual control and the MATLAB PSE. *ACM Trans. Math. Softw.* **27**, 299–316.

KIERZENKA, J. & SHAMPINE, L. F. 2008 A BVP solver that controls residual and error. *J. Numer. Anal. Ind. Appl. Maths* **3**, 27–41.

LOWE, M. & GOLLUB, J. P. 1985 Solitons and the commensurate–incommensurate transition in a convective nematic fluid. *Phys. Rev.* **A31**, 3893–3897.

LYUBIMOV, D. V. & SHKLYAEV, S. V. 2002 Weakly nonlinear analysis of convection of a two-layer system with a deformable interface. *Fluid Dyn.* **37**, 545–555.

MANOR, A., HAGBERG, A. & MERON, E. 2008 Wave-number locking in spatially forced pattern-forming systems. *Europhys. Lett.* **83**, 10005.

MANOR, R., HAGBERG, A. & MERON, E. 2009 Wave number locking and pattern formation in spatially forced systems. *New J. Phys.* **11**, 063016.

MCCOY, J. H., BRUNNER, W., PESCH, W. & BODENSCHATZ, E. 2008 Self-organization of topological defects due to applied constraints. *Phys. Rev. Lett.* **101**, 254102.

NIXON, M., RONEN, E., FRIESEM, A. & DAVIDSON, N. 2013 Observing geometric frustration with thousands of coupled lasers. *Phys. Rev. Lett.* **110**, 184102.

PAL, D. & KELLY, R. E. 1979 Three-dimensional thermal convection produced by two-dimensional thermal forcing. In *Proceedings of Joint ASME/AIChE 18th Natl Heat Transfer Conf.*, pp. 1–8. ASME, 79-HT-109.

SCHMITZ, R. & ZIMMERMAN, W. 1996 Spatially periodic modulated Rayleigh–Bénard convection. *Phys. Rev.* E **53**, 5993–6011.

SEIDEN, G., WEISS, S., MCCOY, J. H., PESCH, W. & BODENSCHATZ, E. 2008 Pattern forming system in the presence of different symmetry-breaking mechanisms. *Phys. Rev. Lett.* **101**, 214503.

SMITH, M. K. & DAVIS, S. H. 1983 Instabilities of dynamic thermocapillary liquid layers. Part 1. Convective instabilities. *J. Fluid Mech.* **132**, 119–144.

VOZOVOI, L. P. & NEPOMNYASHCHY, A. A. 1974 Convection in a horizontal layer in the presence of spatial modulation of temperature at the boundaries. *Gidrodynamika* **7**, 105–117.